

## Effects of repeated hydraulic loads on microstructure and hydraulic behaviour of a compacted clayey silt

Azizi, Arash; Musso, Guido; Jommi, Cristina

**DOI**

[10.1139/cgj-2018-0505](https://doi.org/10.1139/cgj-2018-0505)

**Publication date**

2020

**Document Version**

Accepted author manuscript

**Published in**

Canadian Geotechnical Journal

**Citation (APA)**

Azizi, A., Musso, G., & Jommi, C. (2020). Effects of repeated hydraulic loads on microstructure and hydraulic behaviour of a compacted clayey silt. *Canadian Geotechnical Journal*, 57(1), 100-114. <https://doi.org/10.1139/cgj-2018-0505>

**Important note**

To cite this publication, please use the final published version (if applicable). Please check the document version above.

**Copyright**

Other than for strictly personal use, it is not permitted to download, forward or distribute the text or part of it, without the consent of the author(s) and/or copyright holder(s), unless the work is under an open content license such as Creative Commons.

**Takedown policy**

Please contact us and provide details if you believe this document breaches copyrights. We will remove access to the work immediately and investigate your claim.

1     **Effects of repeated hydraulic loads on microstructure and hydraulic behaviour**  
2                                   **of a compacted clayey silt**

3

4                                   Arash Azizi<sup>1\*</sup>, Guido Musso<sup>2</sup> and Cristina Jommi<sup>3,4</sup>

5

6     \*Corresponding author

7     1. Post-doc Researcher

8     Department of Structural, Geotechnical and Building Engineering

9     Politecnico di Torino

10    Corso Duca degli Abruzzi, 24

11    10129 Torino, Italy

12    [arash.azizi@polito.it](mailto:arash.azizi@polito.it)

13    Currently:

14    Research Fellow

15    Department of Engineering

16    Durham University

17    Lower Mountjoy, South Rd.

18    DH1 3LE Durham, UK

19    [arash.azizi@durham.ac.uk](mailto:arash.azizi@durham.ac.uk)

20    2. Associate Professor

21    Department of Structural, Geotechnical and Building Engineering

22    Politecnico di Torino

23    Corso Duca degli Abruzzi, 24

24    10129 Torino, Italy

25    [guido.musso@polito.it](mailto:guido.musso@polito.it)

26    3. Professor

27    Department of Civil and Environmental Engineering,

28    Politecnico di Milano

29    Piazza Leonardo da Vinci, 32

30    20133 Milano, Italy

31    [cristina.jommi@polimi.it](mailto:cristina.jommi@polimi.it)

32    4. Professor

33 Department of Geosciences and Engineering

34 Delft University of Technology

35 Stevin weg 1

36 2628CN Delft, The Netherlands

37 [c.jommi@tudelft.nl](mailto:c.jommi@tudelft.nl)

38

39 **Abstract**

40

41 Soils used in earth constructions are mostly unsaturated, and they undergo frequent drying-wetting cycles (repeated  
42 hydraulic loads) due to changes in climatic conditions or variations of the ground water level, particularly at shallow  
43 depths. After compaction, changes in water content can significantly influence the hydromechanical response of the  
44 construction material, which therefore has to be assessed for repeated hydraulic loads. This research investigates the  
45 effect of such loads on the microstructure and hydraulic behaviour of a silty soil, typically used in the construction of  
46 embankments and dykes, with the aim of providing a better understanding of the consequences of drying-wetting cycles  
47 on the response of the material over time. Experimental tests were performed to study the impact of drying-wetting  
48 cycles on the water retention, hydraulic conductivity and fabric of compacted specimens. Fabric changes are  
49 documented to take place even without significant volumetric strains, promoting an irreversible increase in the  
50 hydraulic conductivity and a reduction in the capacity to retain water compared to the as-compacted soil. The fabric  
51 changes are interpreted and quantified by means of a hydromechanical model, which accounts for the evolving pore size  
52 distribution at different structural levels. The proposed model reproduces quite well the microstructural observations,  
53 together with the evolution of the water retention behaviour and of the hydraulic conductivity.

54

55

56

57 **Key words:**

58 Compacted silt; drying-wetting cycle; water retention; hydraulic conductivity; microstructure; hydromechanical model

59

60

61

62

63

64

65

66

67

68

69

70

71

72

73

74 Number of words: 7350

75 Number of figures: 13

76 Number of tables: 6

77

78

## 80 1. Introduction

81 Earth structures are widely exposed to interactions with the environment, especially to variations in the atmospheric  
82 conditions and in the ground water level. When the environmental conditions become severe, failure of these structures  
83 may occur causing economic losses and casualties. Far from failure, atmospheric changes and water level oscillations  
84 constitute repeated hydraulic loads inducing drying-wetting cycles, which significantly affect the geotechnical  
85 behaviour of earth structures and slopes because of their impact on the distribution of water pressure (e.g. Vaughan et  
86 al. 2004; Smethurst et al. 2006; Rouainia et al. 2009).

87 Soil-atmosphere interactions are mainly due to precipitations and to seasonal variations of air relative humidity and  
88 temperature. These processes may lead to substantial changes in soil water content and suction, particularly within  
89 superficial soil layers (e.g. Croney 1977; Albright et al. 2004; Smethurst et al. 2006). Calabresi et al. (2013) monitored  
90 the suction and the water content within a soil embankment at Viadana, along the Po River in the North of Italy. In  
91 proximity of the phreatic surface, a zone deeply influenced by the level of impounded water and by capillarity  
92 phenomena, very small variations in suction and moisture content occurred. Instead, suction and water content  
93 oscillated between extreme values in superficial layers, mainly due to Relative Humidity (*RH*) changes in air (between  
94 30 % and 100 %) during the inspection time period (April to October 2001). Such *RH* oscillations represent hydraulic  
95 loads that can significantly influence the efficiency of dykes, embankments and also of covers of waste contaminant  
96 landfills consisting of soils compacted with high compaction efforts (e.g. Daniel 1987). Benson et al. (2007)  
97 characterized the hydraulic behaviour of soils used for water balance covers at the time of construction and a few years  
98 after placement. Over time, generally the hydraulic conductivity increased and the air entry value decreased. Similar  
99 effects on the hydraulic behaviour of unsaturated soils have been related to desiccation cracks (Drumm et al. 1997;  
100 Albrecht and Benson 2001), to freeze-thaw cycles (Benson et al. 1995; Chapuis 2002), and to plant root growth  
101 (Smethurst et al. 2006). For all cases, the detected changes in the hydraulic behaviour suggest void ratio and/or fabric  
102 evolution.

103 The assessment of the long-term behaviour of low activity compacted soils is fundamental to properly understand and  
104 predict the performance of geotechnical structures, such as dykes and embankments, which are mostly built with these  
105 materials. However, little attention has been paid to the effects of hydraulic loading on the fabric and hydraulic  
106 behaviour of low activity compacted soils, while many works have studied these effects for compacted soils of  
107 moderate to high activity (e.g. Sharma 1998; Alshihabi et al. 2002; Cui et al. 2002; Fleureau et al. 2002; Lloret et al.  
108 2003; Alonso et al. 2005; Cuisinier and Masrouri 2005; Nowamooz and Masrouri 2009; Airò Farulla et al. 2010;  
109 Romero et al. 2011).

110 This paper aims to investigate the evolution of the hydraulic behaviour and of the microstructure of a low activity silty  
111 soil exposed to drying-wetting cycles such as those expected to act on superficial soil layers in temperate climates.

112

## 113 **2. Soil properties**

114 The tested soil, collected at Viadana (North Italy), is a clayey silt (grain size distribution in Fig. 1) and it was used in the  
115 construction of an experimental embankment for the assessment of earth structures aimed at the containment of floods  
116 along the Po river. The same material has been previously studied by different authors (e.g. Nocilla et al. 2006; Vassallo  
117 et al. 2007; Calabresi et al. 2013; Azizi et al. 2017).

118 The soil retrieved from different places on site can contain different percentages of clay and sand. The Atterberg limits,  
119 grain specific gravity, calcite content, and grain size distribution of the Viadana silt samples used in this investigation  
120 are listed in Table 1. The material can be classified as low plasticity silt (ML) according to ASTM D2487, with a  
121 plasticity index equal to  $PI = 8.3\%$ . The activity index is  $A = 0.4$ , a value typical of low activity soils.

122 According to X-ray diffraction, the main mineralogical constituents are quartz, calcite and clay minerals of low to  
123 moderate activity (mainly kaolinite, chlorite and illite).

124

## 125 **3. Specimen preparation and drying-wetting cycles**

126 The collected material was dried and mechanically ground. The specimens were prepared by statically compacting the  
127 soil at a dry density  $\rho_d = 1680 \text{ kg/m}^3$  and at a gravimetric water content  $w = 20 \%$ . For each specimen, the dry soil  
128 powder was initially sprayed and hand-mixed with demineralised water according to the target water content, sealed in  
129 plastic bags and kept hanging over distilled water in a sealed humid container for 48 hours allowing water content  
130 equilibration. The wet soil was then placed in a rigid ring having a diameter of 50 mm. An axial force was gradually  
131 applied until the desired height (20 mm) was achieved. To avoid the generation of excess pore pressure that might affect  
132 homogeneity, a low rate of axial displacements (0.15 mm/min) was imposed during loading. After compression, the  
133 specimen was sealed with an impermeable plastic film and kept hanging over distilled water in a closed container for  
134 the following 24 hours to allow for water content equilibration. No significant water content changes occurred during  
135 this stage. The water content and the dry density of the specimens are similar to those adopted in situ for the  
136 experimental embankment (Rojas et al. 2010).

137 Six specimens were used to characterise the microstructure and to study the hydraulic behaviour after compaction. Their  
138 dry density ( $\rho_d$ ), water content ( $w$ ), void ratio ( $e$ ), degree of saturation ( $S_r$ ) and suction ( $s$ ) are reported in Table 2. Other  
139 eight specimens were used to study the effects of repeated hydraulic loads on the water retention, hydraulic conductivity

140 and microstructure. These specimens were subjected to 3 and 6 drying-wetting cycles, namely, “3D/W” and “6D/W”.

141 Drying was imposed by placing the specimens within the holder ring above a rigid mesh. Evaporation of water occurred

142 across the mesh and towards the laboratory environment, at controlled temperature and relative humidity. The

143 temperature was  $T = 21^{\circ}\text{C} (\pm 0.5^{\circ}\text{C})$ . The relative humidity was double-checked and measured to be around  $RH =$

144  $38.5\%$  (the combination of relative humidity and temperature corresponds to a total suction  $\psi = 129$  MPa according to

145 the psychrometric law). The weight and the height of the specimens were measured to track changes in water content

146 and volume. For each of the drying steps, the water content decreased until equilibrium was established after about 120

147 hours, reaching the same value of  $w = 0.38\%$  at the end of all cycles. During drying, an axial stress of 10 kPa was

148 applied. No significant radial strains were induced and shrinkage of the specimen occurred uniaxially.

149 Wetting took place in the same mould used for static compaction, through a plastic porous disc at the bottom, which

150 was connected to a water pressure line to introduce water into the specimen. A small pressure head of 5 kPa was

151 imposed to maintain the pressure gradient adequately low, thus minimising possible effects of transient high water

152 pressures on the soil volume and microstructure. Water filled the pores gradually while the air was escaping through a

153 tiny passage conduit at the top of the mould. The mass of water injected was measured with a water volume indicator

154 and the average injection rate was about  $500\text{ mm}^3/\text{h}$ . Wetting was stopped when the water content of the specimens was

155 equal to the one at compaction ( $w = 20\%$ ). Vertical displacements were allowed during wetting while radial ones were

156 constrained by the holder ring. After the drying-wetting cycles, the specimens were wrapped up in plastic bags and kept

157 hanging over distilled water in a closed container for at least 5 days to ensure water content homogenization. The size of

158 each specimen was then measured. Fig. 2 shows the evolution of water content with time along one drying-wetting

159 cycle.

160 The filter paper technique was used to measure suction after compaction and after the drying-wetting cycles. The

161 calibration curve of Leong et al. (2002) was adopted. The measurements were very consistent with the water retention

162 data of these specimens (see section 5.1 for comparison). The average measured suction of as-compacted specimens

163 was  $s = 33$  kPa, whereas the one of 6D/W specimens was  $s = 5$  kPa.

164

### 165 3.1 Mechanical response during drying-wetting cycles

166 Fig. 3 shows the volume strains  $\varepsilon_v$  and water content  $w$  of the 3D/W and 6D/W specimens as a function of the number

167 of cycles. First drying caused a relatively small shrinkage. The contractive volumetric strains at the end of drying

168 increased during the first two or three cycles, implying some irreversible volumetric strains, and they were almost

169 constant at the end of the following cycles during which the specimens showed nearly reversible behaviour. Negative

170 strains (expansion) were evident at the end of the first wetting stage, despite the water content being the same as  
171 preparation. The expansion strains also stabilized after three cycles.

172

#### 173 4. Experimental methods

174 The hydraulic behaviour and the fabric evolution were studied by different tests, using the techniques summarised in  
175 Table 3. Water Retention Curves (WRC) were determined imposing matric suction  $s$  with the axis translation technique  
176 ( $s \leq 400$  kPa) and imposing total suction  $\psi$  with the vapour equilibrium technique ( $\psi \geq 3$  MPa). The axis translation  
177 technique was adopted in a suction controlled oedometer, where an axial net stress  $\sigma_{net} = 50$  kPa was applied. A  
178 sequence of matric suction  $s = 10, 50, 200, 300, 350$  and  $400$  kPa was imposed over drying. The specimens were then  
179 removed from the oedometer and placed in a desiccator with saturated salt solutions, whose total suctions at the  
180 laboratory temperature were measured with a WP4 Dewpoint Potentiometer. The following total suctions were  
181 imposed:  $\psi = 3.6, 8.8, 21.8, 40.1$  and  $82$  MPa (using the saturated  $K_2SO_4, KNO_3, KCl, NaNO_3$  and  $Ca(NO_3)_2 \cdot 4 H_2O$   
182 solutions, respectively). An axial net stress of  $20$  kPa was imposed during this phase. For each imposed  $\psi$ , the  
183 specimens were kept in the desiccator until equilibrium was established. Their weight and volume were sequentially  
184 measured. After equilibrium at  $\psi = 82$  MPa, wetting was induced by imposing the same suctions of the drying path in  
185 reversed order. The water retention data are hereby presented in terms of matric suction. The matric suction  $s$  was  
186 obtained as the difference between the total suction  $\psi$  and the osmotic suction  $\pi$  for each stage where the vapour  
187 equilibrium technique was applied. The osmotic suction was evaluated as follows: one specimen at the initial water  
188 content and void ratio was squeezed (Iyer 1990) to expel a mass of pore water sufficient for electrical conductivity  
189 measurements. The electrical conductivity of the pore water was  $E.C. = 3.70$  mS/cm, which is consistent with a  
190 molarity  $M = 0.039$  mol/l of a NaCl solution. For each stage of the Vapour Equilibrium path, the actual molarity was  
191 evaluated assuming that only water evaporates, so that the ratio of the dissolved salt mass to the solid fraction of the soil  
192 remains constant. This molarity was converted into electrical conductivity - accounting for the decrease of the mobility  
193 of ions in concentrated solutions. For each stage,  $\pi$  was related to the estimated electrical conductivity through the  
194 graph reported by Fredlund and Rahardjo (1993) (originally from USDA Agricultural Handbook 1950), which was  
195 fitted with the relationship  $\pi = 31.9 \times E.C.^{1.07}$  (units kPa and mS/cm). The empirical relationship between the osmotic  
196 suction and the water content for the tested specimens was then found to be  $\pi = 70.29 \times w^{-1.06}$  ( $w$  is non-dimensional).  
197 The hydraulic conductivity of the saturated specimens was obtained by means of constant head permeability tests. The  
198 specimens were saturated by injecting water while the hydraulic head was kept constant until a steady flow of water

199 took place. The hydraulic conductivity in unsaturated conditions was determined by back analysis of the water content  
 200 changes measured during the water retention tests.

201 Insights on the fabric of specimens at different states were provided by Pore Size Distribution (PSD) curves and by  
 202 direct observations with Environmental Scanning Electron Microscope (ESEM) pictures. The PSD curves were  
 203 determined through Mercury Intrusion Porosimetry (MIP) carried out using a Micromeritics AutoPore IV 9500, in  
 204 which two different systems were operated: a low mercury pressure system (between 0 and 0.345 MPa) and a high  
 205 mercury pressure system (between 0.345 MPa and 228 MPa). These operating systems allow mercury to intrude pores  
 206 with radii ranging between 0.0035  $\mu\text{m}$  and 200  $\mu\text{m}$ . Cylindrical specimens with height and diameter of 10 mm were  
 207 trimmed from the original ones for MIP analyses. The fabric of the wet specimens was preserved by dehydration using  
 208 the freeze-drying technique (Delage and Pellerin 1984). All specimens were then weighted and placed in the  
 209 penetrometer, followed by evacuation of gas from the chamber to generate the vacuum condition.

210

## 211 **5. Effects of repeated hydraulic loads on the hydraulic behaviour**

### 212 **5.1 Water retention behaviour**

213 Fig. 4(a) shows the water retention curves of the as-compacted specimens and of the specimens subjected to drying-  
 214 wetting cycles in terms of  $\log(s)$ - $S_r$ . A reduced capacity for retaining water of the D/W specimens was evident along  
 215 both the main drying and the main wetting paths, where the water content of the D/W specimens was always noticeably  
 216 smaller than that of the as-compacted specimen for suction  $s < 20$  MPa. Drying-wetting effects were not observed at  
 217 very high suction ( $s \geq 20$  MPa). Consistently with the reversible mechanical response after the third drying-wetting  
 218 cycle, the drying WRC of the 6D/W specimen was quite similar to the one of the 3D/W specimen. Volume changes  
 219 taking place during the water retention tests were very small.

220 The initial void ratio of the D/W specimens was slightly smaller than the one of the as-compacted specimens because  
 221 the formers had a slightly higher volume decrease under the axial net stress  $\sigma_{net} = 50$  kPa imposed in the suction  
 222 controlled oedometer. Volume changes taking place during the water retention tests were very small (Fig. 4(b)).  
 223 Altogether, the results showed that the water retention behaviour of the D/W specimens differs from the original one  
 224 mainly because of changes in the soil fabric, mostly occurring during the first cycles, rather than because of changes in  
 225 the void ratio.

226 Different water retention domains can be identified: a high suction range with almost no hysteresis ( $s \geq 20$  MPa), an  
 227 intermediate suction range and a low suction range, which can be distinguished from each other by substantial changes  
 228 in the shape of the curves as shown in Fig. 4(c) in terms of water ratio ( $e_w = S_r \cdot e$ ) and suction. The size of the two latter

229 domains, which are separated by the inflection point of the WRC, evolved during the drying-wetting cycles (see also  
 230 Romero and Vaunat 2000; Aubertin et al. 2003; Romero et al. 2011; Della Vecchia et al. 2015).

231

## 232 5.2 Hydraulic conductivity

233 The average saturated hydraulic conductivity of the specimens, evaluated by constant head tests, was  $K_s = 1.1 \times 10^{-9}$  m/s  
 234 for the as-compacted specimens and  $K_s = 1.3 \times 10^{-8}$  m/s for the 6D/W specimens. The hydraulic conductivity in  
 235 unsaturated conditions was determined by back analysis of the water content changes measured during the water  
 236 retention tests. The Finite Element code COMSOL was used to reproduce the water outflow along the suction  
 237 equalization phases of the drying paths (in the range  $10 \leq s \leq 400$  kPa) and the hydraulic conductivity was then obtained  
 238 relying on Richard's equation (e.g. Eching et al. 1993; van Dam et al. 1994; Fujimaki and Inoue 2003):

$$239 \quad \frac{\partial \theta}{\partial t} = - \frac{\partial K_w(S_e)}{\partial z} \frac{\partial s}{\gamma_w} \left[ \frac{\partial s}{\partial z} - 1 \right] \quad (1)$$

240 where  $\gamma_w$  is the specific weight of water,  $\theta = \frac{e_w}{1+e}$  is the volumetric water content,  $z$  is the spatial coordinate,  $t$  is the  
 241 time and  $K_w$  is the hydraulic conductivity in unsaturated conditions. The effective degree of saturation  $S_e$  is defined as  
 242  $S_e = \frac{S_r - S_{res}}{1 - S_{res}}$ , where  $S_{res} = 0.07$  is the residual degree of saturation. For each suction increment, the decrease in water  
 243 content was expressed in terms of moisture capacity  $C(s) = \frac{\partial \theta}{\partial s}$  determined from the WRC and the current hydraulic  
 244 conductivity was approximated with its average constant value. The following equation was then solved:

$$245 \quad C(s) \frac{\partial s}{\partial t} = - \frac{K_w(S_e) \partial^2 s}{\gamma_w \partial z^2} \quad (2)$$

246 An optimization procedure was implemented to determine the best values of  $K_w$  for the as-compacted and 6D/W  
 247 specimens. In the experiments, the water flow rate depended also on the impedance of the bottom porous stone, through  
 248 which the flow took place. Therefore, the porous stone, having height 7 mm and saturated hydraulic conductivity  
 249  $1.21 \times 10^{-9}$  m/s, was also modeled. In the numerical simulation, suction values were imposed at the bottom of the porous  
 250 stone, while a no flow condition was imposed at the top boundary.

251 Fig. 5(a) compares the changes in the volumetric water content  $\Delta \theta$  measured during the test with the numerical  
 252 predictions. According to the back analysis, the hydraulic conductivity of the 6D/W specimen is greater than the one of  
 253 the as-compacted specimen over the whole saturation range (Fig. 5(b)). This general increase of hydraulic conductivity,  
 254 observed also at full saturation, is related to the fabric changes taking place at almost constant volume, which are  
 255 discussed in detail in the following.

256

257 **6. Effects of repeated hydraulic loads on microstructure**258 **6.1 Fabric arrangement**

259 ESEM pictures of the as-compacted and 6D/W specimens shown in Figs. 6(a), 6(b) and 6(c) portray the soil fabric and  
 260 the pore network. These pictures were taken while setting the temperature  $T = 10$  °C and the vapour pressure  $u_v = 630$   
 261 Pa in the chamber, with a corresponding relative humidity  $R.H. = 53\%$ . The silt and clay fractions are well evident. The  
 262 clay fraction consists of single clay particles (denoted by ‘C’) and of aggregations of clay particles (clay peds). Silt  
 263 particles (denoted by ‘S’) are also evident.

264 The radii of the pores between peds and between large particles and peds, recognised at the lower magnification of Figs.  
 265 6(a), 6(b) and 6(d), are of the order of a few microns. The radii of the pores within the peds appear to be clearly below 1  
 266  $\mu\text{m}$  including those recognised at the higher magnification of Fig. 6(c) and those invisible at this magnification. This  
 267 may suggest three classes of pores including micropores and mesopores inside the peds and macropores external to the  
 268 peds, as it will be discussed in the next section.

269 Fig. 6(d) shows an ESEM image of the 6D/W dry specimen. This figure shows that single peds might break into smaller  
 270 peds, separated by fractures having the size of macropores, which suggests that drying-wetting cycles induce breakage  
 271 of peds, increasing the macroporosity. Nonetheless, neither cracks nor fissures at the surface of the specimens were  
 272 evident to the naked eye.

273

274 **6.2 Pore size distribution**

275 The pore size distributions presented in Fig. 7(a) describe the following four conditions: As-compacted ( $w = 20\%$ ), after  
 276 first drying (‘As-compacted dry’,  $w = 0.38\%$ ), at the end of the sixth drying stage (‘6D/W dry’) and at the end of the  
 277 sixth wetting stage (‘6D/W’). The PSD curves are clearly bi-modal, with a dominant peak in correspondence of a pore  
 278 radius smaller than 1  $\mu\text{m}$  and another peak in the range of 5-10  $\mu\text{m}$ . Microstructural changes from the as-compacted  
 279 condition to the 6D/W condition are evident. The as-compacted and the as-compacted dry specimens have a dominant  
 280 pore radius  $r = 609$  nm, but the size of the peak is greater for the dry specimen. The PSDs of the 6D/W dry and 6D/W  
 281 specimens overlap very well, both showing an increase of the dominant pore radius to  $r = 917$  nm. The radius of the  
 282 smaller PSD peak shifts from about 5  $\mu\text{m}$  (as-compacted) to about 8  $\mu\text{m}$  (wet state of the 6D/W), while it remains about  
 283 5  $\mu\text{m}$  for the 6D/W dry. The evolution of the PSDs shows that the soil fabric is sensitive to repeated hydraulic loads,  
 284 confirming that fabric changes take place even without significant changes in the total volume.

285 The total intruded void ratio  $e_{int}$  was smaller than the total void ratio  $e$  (Fig. 7(b)) since not all the available porosity was  
 286 intruded by mercury. This difference is due both to very large pores, filled by mercury at very low pressures, whose

287 volume is not measured during intrusion, and to very small pores which are not intruded even at very high pressures.  
 288 The fraction of void ratio associated to the very small pores is assumed to be equal to the water ratio corresponding to  
 289 irreducible saturation, and it is about 0.04 for all specimens. The non-intruded fraction of void ratio associated with very  
 290 large pores is then estimated as the difference between the non-intruded void ratio and 0.04.  
 291 Based on the PSDs, three classes of pores (micropores, mesopores and macropores) are identified. This allows  
 292 individuating a microstructural void ratio  $e_{Mi}$ , a mesostructural void ratio  $e_{Me}$  and a macrostructural void ratio  $e_{Ma}$ :

$$e_{Mi} = \frac{V_{vMi}}{V_s}, e_{Me} = \frac{V_{vMe}}{V_s}, e_{Ma} = \frac{V_{vMa}}{V_s} \quad (3)$$

293 where  $V_{vMi}$  is the volume of the micropores,  $V_{vMe}$  is the volume of the mesopores,  $V_{vMa}$  is the volume of the macropores  
 294 and  $V_s$  is the volume of the solid phase. The total void ratio  $e$  is then:

$$e = e_{Mi} + e_{Me} + e_{Ma} \quad (4)$$

296  
 297 Selecting a criterion to discriminate between different classes of pores always involves some degree of arbitrariness,  
 298 and the choices that were made in the elaboration of the data are presented here. Micropores are defined as those pores  
 299 still saturated at very high suctions, and whose behaviour during drying-wetting cycles is completely reversible. On the  
 300 basis of the results in Fig. 4(c), the corresponding void ratio is  $e_{Mi} = 0.06$  for all conditions. The threshold pore radius  
 301 separating micropores from mesopores  $R_{Mi}$  is determined as the radius at which the following condition is satisfied:

$$e_{Mi} = \int_{3.5}^{R_{Mi}} \frac{PSD(r)}{3.5 r \cdot \ln(10)} dr + 0.04 \quad (5)$$

302 where 3.5 nm is the smallest pore radius intruded by MIP and 0.04 is the void ratio corresponding to the very small non  
 303 intruded pores. By imposing  $e_{Mi} = 0.06$  it follows  $R_{Mi} = 11$  nm. Note that the argument function of the integral in eq. (5)  
 304 follows logically from the definition of the PSD as the incremental fraction of intruded void ratio with respect to the  
 305 logarithm of the pore radius, as discussed for instance by Della Vecchia et al. (2015).

306  
 307 Mesopores are identified with the larger pores within the clay peds. According to the ESEM pictures (Fig. 6), their radii  
 308 are expected to be smaller than 1  $\mu\text{m}$ . MIP analyses of specimens loaded to increasingly higher net stresses showed a  
 309 progressive reduction of the volume of the pores having radii greater than the dominant peak, and no clear effects on  
 310 pores whose radius was smaller (Azizi et al. 2018). The evidence confirms the shared view that mechanical  
 311 compression mostly affects pores external to clay aggregates (or macro-pores, see e.g. Delage and Lefebvre 1984;  
 312 Tarantino and De Col 2008; Koliji et al. 2010). Therefore, the threshold pore radius  $R_{Me}$  separating the macropores from  
 313 the mesopores was selected as the pore radius of the dominant peak of the PSD (equal to 609 nm for the as-compacted  
 314 and first drying states, and equal to 917 nm for the 6D/W dry and 6D/W wet states).  $V_{vMe}$  is the volume of pores whose

315 entrance radius is between  $R_{Mi}$  and  $R_{Me}$ ; the values of  $e_{Me}$  were obtained through Eq. (3). Finally, values of  $e_{Ma}$  for each  
 316 state were determined by applying Eq. (4).

317 The threshold pore radii separating the different classes of pores and the void ratios  $e_{Mi}$ ,  $e_{Me}$  and  $e_{Ma}$  are summarised in  
 318 Table 4.

319

### 320 6.3 Fabric evolution based on conjugate analysis of MIP and ESEM data

321 Repeated hydraulic loads induce two different effects at the mesostructural level. Firstly, the mesostructural void ratio  
 322 of the 6D/W states ( $e_{Me} = 0.32$ ) is smaller than the one of the as-compacted state ( $e_{Me} = 0.36$ ). This suggests that the peds  
 323 experience irreversible strains, and their contraction during drying is not fully recovered during wetting. Since the final  
 324 suction is smaller than the one at preparation, the behaviour of the peds cannot be elastic, otherwise drying-wetting  
 325 cycles would lead to a net expansion of the peds. Secondly, the radius of the larger mesopore increases from 609 nm to  
 326 917 nm (Table 4).

327 While the overall void ratio remains constant upon the repeated hydraulic loads, the macrostructural void ratio evolves  
 328 from the initial  $e_{Ma} = 0.24$  of at the as-compacted state to  $e_{Ma} = 0.28$  of the 6D/W wet state. Simultaneously, the  
 329 dominant radius of macropores increases from 5030 nm to 8230 nm. Contraction of the peds is responsible for larger  
 330 macroporosity and larger individual macropores, thanks to stiffening effect of the granular silt skeleton, which is less  
 331 sensitive to water content changes (as observed also for Barcelona clayey silt by Romero et al. 2014). The lower air  
 332 entry value of the peds, the larger macrostructural void ratio and the larger pore radii of the macrostructure of 6D/W  
 333 samples all concur to explain the significant change of the water retention capacity and the increase in hydraulic  
 334 conductivity.

335 The experimental WRCs and those predicted on the basis of MIP results are compared in Fig. 8. Since mercury is a non-  
 336 wetting fluid, MIP data can be used to derive a water retention curve by assuming that its penetration is equivalent to air  
 337 intrusion during a drying path. The radius  $r$  of a pore determines both the matric suction  $s$  during drying and the  
 338 pressure of penetrating mercury  $p$  (e.g. Romero et al. 1999), so that:

339

$$s = \frac{4\sigma\cos\theta_w}{r}; p = -\frac{4\sigma_{Hg}\cos\theta_{Hg}}{r}; s = -\frac{\sigma\cos\theta_w}{\sigma_{Hg}\cos\theta_{Hg}}p \approx 0.196 p \quad (6)$$

340 where  $\sigma = 0.072$  N/m is the surface tension of water and  $\theta_w = 0^\circ$  is the contact angle for the air-water interface,  $\sigma_{Hg} =$   
 341 0.484 N/m is the surface tension of mercury and  $\theta_{nw} = 140^\circ$  is the contact angle between mercury and the particle  
 342 surface.

343 The WRC is derived from MIP data at the fixed void ratio of the tested sample. On the contrary, single values of water  
344 retention determined experimentally over drying/wetting paths reflect the concomitant shrinkage and swelling occurring  
345 during the test. Direct comparison of the two is hardly significant in the case of active clays (Romero et al. 2011), for  
346 which numerous PSDs are required to determine the complete retention domain (Della Vecchia et al. 2015). However,  
347 in the case of Viadana silt changes in total void ratio are negligible, and the MIP derived WRCs reproduce quite well  
348 the experimental water retention both along first drying and along drying after 6D/W cycles. The difference between the  
349 first drying and the following drying paths shows the relevance of internal microstructural rearrangement for the tested  
350 silty soil, though its composition include no relevant percentage of active clay minerals particularly sensitive to  
351 physico-chemical phenomena.

352

## 353 7. Modelling macroscopic behaviour accounting for microstructural evolution

### 354 7.1 Coupled hydromechanical model

355 The experimental results show that both the hydraulic behaviour and the fabric of Viadana silt evolve with drying-  
356 wetting cycles. The volume of the peds and the water retention properties undergo irrecoverable changes during the first  
357 cycle, and stabilise afterwards. To assist in the interpretation of the data and to quantify the effects of the drying-wetting  
358 cycles, a microstructural framework is needed. Table 4 suggests that the microstructural void ratio  $e_m$  remained  
359 constant, so it is not strictly necessary to consider the micro-pores separately from the meso-pores when formulating a  
360 microstructural model, since both classes of pores are found within the peds. A double porosity framework was then  
361 used which allows to distinguish between the micro-meso and the macro fabric levels and to incorporate microstructural  
362 changes.

363 A model for the volumetric response is introduced to this extent. Two structural levels are defined and described based  
364 on their respective void ratios, one pertaining to the void space within the peds (intra-peds) and the other external to the  
365 peds (macrostructure). The overall behaviour of the material follows as the superposition of the two structural levels  
366 where the two fabric levels are assumed to be in hydraulic and mechanical equilibrium. Two sets of hydromechanical  
367 variables are defined: matric suction and Bishop type effective stress as stress variables, and water ratio (or degree of  
368 saturation) and volume strain (or void ratio) as strain variables. The proposed model shares fundamental hypotheses  
369 with double porosity models formulated for expansive soils (e.g. Gens and Alonso 1992; Alonso et al. 1999; Mašin  
370 2013, Musso et al. 2013) whereas it adopts the elastoplastic framework for the behaviour of the peds based on the  
371 microstructural observations. The asymptotic behaviour resulting from an increasing number of drying-wetting cycles is  
372 then reproduced as a direct consequence of the proposed hardening laws, which are discussed in the following.

373

### 374 7.1.1 Fabric levels and strain variables

375 Micropores and mesopores belong to the intra-peds porosity, while macro-pores are associated with the porosity  
376 external to the peds. The intra-peds void ratio  $e_m$  and the macrostructural void ratio  $e_{Ma}$  are defined as:

$$e_m = e_{Me} + e_{Mi} = \frac{V_{vMe} + V_{vMi}}{V_s} = \frac{V_{vm}}{V_s}, e_{Ma} = \frac{V_{vMa}}{V_s} \quad (7)$$

377 where  $V_{vm}$  is the volume of the intra-peds voids.

378 The intra-peds water ratio  $e_{wm}$  and the macrostructural water ratio  $e_{wMa}$  are obtained imposing that the total mass of  
379 water stored within the soil is the sum of the mass of water within the peds and the mass of water in the macroporosity:

$$e_w = e_{wMa} + e_{wm} = e_{Ma}S_{rMa} + e_mS_{rm} \quad (8)$$

380

381 with  $e_{wm} = \frac{V_{wm}}{V_s}$ ,  $e_{wMa} = \frac{V_{wMa}}{V_s}$ ,  $S_{rm} = \frac{V_{wm}}{V_{vm}}$ ,  $S_{rMa} = \frac{V_{wMa}}{V_{vMa}}$ , where  $V_{wm}$  is the volume of water within the peds,  $V_{wMa}$  is the  
382 volume of water within the macropores,  $S_{rm}$  is the intra-peds degree of saturation,  $S_{rMa}$  is the macrostructural degree of  
383 saturation.

384

### 385 7.1.2 Stress variables

386 Two stress variables are employed including a mechanical constitutive stress and suction. The first one is assumed to  
387 depend on the net stress ( $\sigma_{net}$ ), the effective degree of saturation ( $S_e$ ) and the suction in the form:

$$\boldsymbol{\sigma}' = \boldsymbol{\sigma}_{net} + S_e s \mathbf{I} \quad (9)$$

388 where Eq. (9) is a general expression, which can be used to describe the average mechanical stress acting on the soil  
389 skeleton or on each structural level (macrostructural stress  $\boldsymbol{\sigma}'_{Ma}$  or peds stress  $\boldsymbol{\sigma}'_m$ ), by using the corresponding effective  
390 degree of saturation. As in most of the previous double porosity models, the total (net) stress acting on each level is  
391 assumed to be the same (e.g. Alonso et al. 1999; Mašin 2013; Wang et al. 2015). The second stress variable is the  
392 matric suction. Similar stress variables have been adopted by different authors (e.g. Jommi 2000; Romero and Jommi  
393 2008; Della Vecchia et al. 2013).

394

### 395 7.1.3 Water retention model

396 According to Eq. (8), the overall WRC in terms of water ratio  $e_w(s)$  is expressed as the superposition of the WRCs of  
397 the two fabric levels (e.g. Durner 1994; Casini et al. 2012; Della Vecchia et al. 2015):

$$e_w(s) = e_{Ma} \left[ \frac{1}{1 + (\alpha_{Ma} s)^{n_{Ma}}} \right]^{m_{Ma}} + e_m \left[ \frac{1}{1 + (\alpha_m s)^{n_m}} \right]^{m_m} \quad (10)$$

398 where  $n_{Ma}$ ,  $m_{Ma}$ ,  $\alpha_{Ma}$  and  $n_m$ ,  $m_m$ ,  $\alpha_m$  are the parameters of the van Genuchten's model (1980) for macro-pores and  
 399 intra-peds pores, respectively. The total degree of saturation is obtained by the sum of  $S_{rMa}$  and  $S_{rm}$  weighted by the  
 400 corresponding volumetric fractions.

401 A relationship between water ratio and suction in the scanning domain is needed for the simulation of the transition  
 402 from drying to wetting branches (and vice versa) over the hydraulic cycles. The incremental form of equation (10)  
 403 reads:

$$de_w(s) = de_{wMa} + de_{wm} = [S_{rMa}de_{Ma} + e_{Ma}dS_{rMa}] + [S_{rm}de_m + e_mdS_{rm}] \quad (11)$$

404  
 405 The scanning curves are predicted by replacing  $dS_r = -k_{sc}ds$  for each structural level:

$$de_w^{sc}(s) = \left[ \frac{e_{wMa}}{e_{Ma}}de_{Ma} - e_{Ma}k_{sc}ds \right] + \left[ \frac{e_{wm}}{e_m}de_m - e_mk_{sc}ds \right] \quad (12)$$

406 where  $k_{sc}$  controls the slope of the scanning curves. The behaviour in the scanning domain is assumed to be reversible.

407

#### 408 7.1.4 Mechanical model

409 Water retention depends on the macrostructural and intra-peds void ratios, whose evolution is predicted by a mechanical  
 410 model. Wheeler et al. (2003) proposed an elastoplastic framework that couples hydraulic hysteresis with stress-strain  
 411 behaviour. A similar framework is adopted to reproduce the mechanical behaviour of the peds coupled with the intra-  
 412 peds water retention. The peds constitutive stress ( $\sigma'_m$ ) is employed to predict the volumetric changes of the peds,  
 413 influenced by the intra-peds effective degree of saturation. On the other hand, intra-peds void ratio changes affect the  
 414 intra-peds water ratio, because both the water storage capacity and the air-entry value evolve.

415 Hardening is introduced including two yielding criteria: one associated with mechanical straining of the peds and the  
 416 other responsible for irreversible changes of the peds water ratio. As shown in Fig. 9(a), the former yielding occurs  
 417 when the stress path reaches the loading collapse (LC) curve whereas the latter is triggered if the stress path reaches the  
 418 suction increase (SI) curve during drying, or the suction decrease (SD) curve during wetting. These yield curves are  
 419 expressed as:

$$\text{LC: } \sigma'_m = \sigma'^*_m, \text{ SI: } s = s_I, \text{ SD: } s = s_D \quad (13)$$

420

421 Where  $\sigma'^*_m$  is the peds yield stress,  $s_I$  is the suction increase yield curve and  $s_D$  is the suction decrease yield curve.

422 Increments of volumetric strains of the peds occurring inside the elastic domain ( $\Delta\varepsilon_m^e$ ) are given by:

$$d\varepsilon_m^e = \frac{\kappa m d\sigma'_m}{(1 + e_m)\sigma'_m} \quad (14)$$

423

424 where  $\kappa_m$  is the elastic compliance for the intra-peds void ratio. For stress paths within the elastic domain, the degree of  
425 saturation evolves along the scanning curves.

426 If yielding occurs directly on the SI, it induces water ratio changes on the main drying WRC accompanied with  
427 hardening of the LC, whereas direct yielding on the SD induces water ratio changes on the main wetting WRC  
428 accompanied with softening of the LC. If yielding occurs on the LC, it produces plastic volumetric strains with a  
429 coupled outward movement of the SI and inward movement of the SD. The SI and the SD evolve together:

$$\frac{ds_I}{s_I} = \frac{ds_D}{s_D} \quad (15)$$

430 When yielding occurs due to SI or SD, the hardening law is:

$$d\sigma'^*_m = h_{lC} \sigma'^*_m \frac{ds_I}{s_I} \quad (16)$$

431  $h_{lC}$  controls the coupled movement of the LC due to SI or SD yielding. The increments of plastic volumetric strains ( $d$   
432  $\varepsilon_m^p$ ) due to yielding of LC curve are

$$d\varepsilon_m^p = \frac{(\lambda_m - \kappa_m) d\sigma'^*_m}{(1 + e_m) \sigma'^*_m} \quad (17)$$

433 where  $\lambda_m$  and  $\kappa_m$  are model parameters and the hardening law in this case is given by,

$$ds_I = h_s s_I \frac{d\sigma'^*_m}{\sigma'^*_m} \quad (18)$$

434 where  $h_s$  controls the coupled movement of SI and SD.

435 The general expression for plastic strain increment can be derived through Eqs. (16) and (17):

$$d\varepsilon_m^p = \frac{(\lambda_m - \kappa_m)}{(1 + e_m)(1 - h_s h_{lC})} \left( \frac{d\sigma'^*_m}{\sigma'^*_m} - h_{lC} \frac{ds_I}{s_I} \right) \quad (19)$$

436

437 Two flow rules are given, respectively associated to the yielding on the SI and SD curves:

$$\frac{d\varepsilon_m^p}{de_{wm}} = 0 \quad (20)$$

438 and associated to the yielding on the LC curve:

$$\frac{de_{wm}}{d\varepsilon_m^p} = 0 \quad (21)$$

439

440 Changes of the intra-peds void ratio are written in the form:

$$de_m = -d\varepsilon_m(1 + e_m) = -(d\varepsilon_m^e + d\varepsilon_m^p)(1 + e_m) \quad (22)$$

441

442 The influence of the mechanical effects on the WRC of the peds is shown in Fig. 9(b). The specimens were subjected to  
 443 a wide range of suction and the peds were almost completely dry at the end of drying, whereas they were entirely  
 444 saturated at the end of wetting. SI yielding occurred when air entered the saturated peds (suction greater than their air-  
 445 entry value), and SD yielding occurred along wetting when the degree of saturation of the peds  $S_{rm}$  was greater than the  
 446 residual one.

447 A similar framework may also be adopted also for the macrostructural fabric level. However, changes of the  
 448 macrostructural void ratio were evaluated here as the difference between the changes of the total void ratio and that of  
 449 the intra-peds void ratio. A simple elastic expression was used for the increments of overall volume strains ( $d\varepsilon_v$ ):

$$d\varepsilon_v = \frac{\kappa \cdot d\sigma'}{(1+e)\sigma'} \quad (23)$$

450 where  $\kappa$  is the elastic logarithm compressibility. Hence, the total void ratio changes are:

$$de = -d\varepsilon_v(1+e) \quad (24)$$

451 and the macrostructural void ratio changes are:

$$de_{Ma} = de - de_m \quad (25)$$

452 Eqs. (22) and (25) give the evolution of the void ratio of macro- and intra-peds pores which contribute to the coupled  
 453 water retention model (Eq. (10)).

454

## 455 7.2 Calibration of the parameters

456 The parameters calibration was mostly based on independent tests with respect to the WRCs reproduced. An oedometer  
 457 test was used to determine the elastic compliances of the overall soil  $\kappa$  and the one of the peds  $\kappa_m$ , which were assumed  
 458 to have the same value of 0.003, and the preconsolidation stress imposed during compaction,  $\sigma'_m = 657$  kPa, which  
 459 identifies the initial position of the LC (see details in Azizi 2016). The initial air entry value of the peds  $1/\alpha_m = 236$  kPa  
 460 was determined by means of the MIP measurements, introducing the radius of the larger mesopore ( $r = 609$  nm) into the  
 461 first one of Eq. 6. According to the model, the air entry value also provides the initial position of the SI, while the SD is  
 462 set equal to the suction imposed at the beginning of the water retention test (SD = 10 kPa). The parameters for the WRC  
 463 of the macro-structure were determined imposing the best fit between the experimental water ratio of the macrostructure  
 464 ( $e_{vMa} = e_w - e_m$ ) along the first drying branch for suction values smaller than the air entry value of the peds (Table 5).  
 465 The elasto-plastic compliance  $\lambda_m$  was calibrated to capture the amount of contraction of the peds during the first drying  
 466 stage, as determined with MIP. The scanning parameter  $k_{sc}$  was calibrated upon water retention tests presented by Azizi  
 467 et al. (2017). The parameters  $h_{LC}$  and  $h_s$  were calibrated to obtain a reversible behaviour after three cycles.

468 The van Genuchten's parameters of both structural levels evolve along the hydraulic cycles to adequately reproduce the  
 469 evolution of the water retention. Simple relationships were chosen relating  $1/\alpha_{Ma}$  and  $1/\alpha_m$  to the saturated water  
 470 ratios of the macropores  $e_{wMa}^{sat}$  and of the peds  $e_{wm}^{sat}$ .

$$1/\alpha_{Ma} = (e_{Ma0}/e_{wMa}^{sat})^4/\alpha_{Ma0} \text{ and } 1/\alpha_m = (e_{wm}^{sat}/e_{m0})^{8.2}/\alpha_{m0} \quad (26)$$

471  
 472 where  $e_{Ma0}$  and  $e_{m0}$  are the initial macrostructural and intra-peds void ratios of the as-compacted specimen, and  $1/\alpha_{Ma0}$   
 473 and  $1/\alpha_{m0}$  are the initial air-entry values of the respective drying curves. The empirical laws described by Eq. (26) were  
 474 used both for the main drying and the main wetting curves. The parameters of the mechanical model are listed in Table  
 475 6.

476 The model was employed to predict the final values of  $\alpha_M$  and  $\alpha_m$ , which determine the WRC after 6 cycles, together  
 477 with the final values of the hydraulic conductivity and of the relative permeability.

478

### 479 7.3 Simulation of drying-wetting cycles: mechanical behaviour and water retention

480 The void ratio and suction measured during the water retention tests are compared to the model predictions in Fig.  
 481 10(a). Six drying-wetting cycles were simulated. The evolution of the intra-peds and macrostructural void ratios is  
 482 presented in Fig. 10(b). Void ratios evaluated on basis of the MIP data are nicely captured. Adopting an elastoplastic  
 483 framework for modeling the behaviour of the peds allowed properly simulating the decrease of the intra-peds void ratio  
 484 and the increase of the macro-structural void ratio occurring during the first 3 hydraulic cycles.

485 The modelled changes in intra-peds and macrostructural void ratios rule the evolution of the water retention, whose  
 486 simulation is introduced in Fig. 11. Fig. 11(a) shows the experimental results and the model predictions for the first  
 487 drying and wetting cycle in terms of  $S_r$ - $\log(s)$ . The predictions of the degree of saturation of the macropores and of the  
 488 peds are also provided. Since different air-entry values are defined for the two structural levels, in the suction range 64  
 489 kPa  $< s < 236$  kPa the peds are still saturated while the macro-pores are desaturating. A similar condition occurs during  
 490 wetting in the suction range 8 kPa  $< s < 34$  kPa. The changes in the WRCs of the two structural levels due to drying-  
 491 wetting cycles are given in Fig. 11(b). At the end of each wetting stage, the intra-peds pores are always fully saturated,  
 492 while, for the same suction, the degree of saturation of the macropores  $S_{rMa}$  decreases during the first three cycles. The  
 493 water retention behaviour of the 6D/W specimens was predicted by simulating 6 drying-wetting cycles imposed to the  
 494 as-compacted specimen, and it is plotted in Fig. 11(c). The good match between experimental data and predictions  
 495 shows the capability of the conceptual model to reproduce the evolution of the water retention behaviour over hydraulic  
 496 cycles.

497 Experimental water retention data of the first drying-wetting cycle and model predictions are re-plotted in Fig. 12(a) in  
 498 terms of  $e_w - \log(s)$ . The water ratio of peds  $e_{wm}$  at the end of the first wetting is smaller than the original one, since the  
 499 intra-peds void ratio reduces due to plastic strains. On the contrary, the water ratio of macropores  $e_{wMa}$  increases. During  
 500 the first three drying-wetting cycles  $e_m$  progressively reduces while  $e_{Ma}$  progressively increases, affecting the air entry  
 501 values of both peds and macropores (Eq. 26). Fig. 12(b) shows the experimental results and model predictions for the  
 502 6D/W specimen. For both structural domains, the water ratio at the beginning of drying and at the end of wetting is the  
 503 same since the mechanical behaviour became reversible and the water retention curves cannot evolve further.

504

505

#### 506 7.4 Model validation exploiting the hydraulic conductivity analysis

507 The hydraulic conductivity of compacted soils having bimodal pore size distribution is mainly related to the volume and  
 508 distribution of the larger pores (e.g. Cuisinier et al. 2011; Romero 2013). As a result, the increase in the saturated  
 509 hydraulic conductivity  $K_s$  evidenced in Section 5.2 is justified by the increase of the macrostructural void ratio and can  
 510 be modeled using a Kozeny-Carman like equation based on  $e_{Ma}$  (Romero 2013):

$$K_s = B \frac{e_{Ma}^5}{1 + e_{Ma}} \quad (27)$$

511

512 where  $B = 5 \times 10^{-6}$  m/s was found to adequately simulate the experimental data. The hydraulic conductivity under  
 513 unsaturated condition  $K_w$  is defined as the product of a relative permeability  $k_r$  and  $K_s$ :

$$K_w = k_r K_s \quad (28)$$

514

515 The relative permeability  $k_r$  is controlled by the size of the pores and the shape of PSD. It can be predicted either from  
 516 the relationships between suction and effective degree of saturation (Mualem 1976):

$$k_r^{(Mualem)} = \frac{K_w}{K_s} = S_e^{1/2} \left[ \frac{\int_0^{S_e} dS_e / s}{\int_0^1 dS_e / s} \right]^2 \quad (29)$$

517

518 or as a power law function of the degree of saturation (e.g. Bear 1972), whose exponent is often assumed equal to 3. By  
 519 admitting that the contribution to flow of the intra-peds pores is negligible, it follows that:

$$k_r^{(Macro)} = \left( \frac{S_r - \frac{e_{wm}}{e}}{1 - \frac{e_{wm}}{e}} \right)^3 \quad (30)$$

520

521 The values of  $S_r$ ,  $e_{wm}$  and  $e$  given by the simulations were introduced in both Eq. (29) and Eq. (30) to obtain the  
 522 predictions presented in Fig. 13(a), where they are compared to the experimental data based on the back-analysis of  
 523 Richards' equation. Both expressions captured the experimental data well, although the prediction of the power law  
 524 expression was found to better match the experimental results.

525 The evolution of  $K_w$  during hydraulic cycles is obtained by combining the hydromechanical model with Eq. (27) and  
 526 Eq. (30). The predictions are compared to the data obtained by the inverse analysis of Richard's equation in Fig. 13(b),  
 527 where a good match is observed. It is worth noting that since the total void ratio changed reversibly during drying-  
 528 wetting cycles, the Kozeny-Carman equation, as well as any other model giving an estimate of the hydraulic  
 529 conductivity based on the total void ratio, would not be able to predict any change in the hydraulic conductivity. On the  
 530 contrary, the framework developed is able to predict the irreversible increase in macroporosity during drying and  
 531 wetting cycles, which resulted in the observed relevant increase in the hydraulic conductivity of the investigated soil  
 532 specimens.

533

## 534 8. Summary and conclusions

535 While the influence of fabric and fabric evolution on the hydromechanical behaviour of compacted active clays has  
 536 been studied in detail in the recent years, its relevance on the hydromechanical behaviour of low activity clays and silts  
 537 has been less explored. These materials are widely used to build earth structures exposed to intensive interaction with  
 538 water and the atmosphere. Assessment of their response to environmental actions is then relevant for the long-term  
 539 stability and serviceability of engineering works. This study was aimed to evaluate the impact of typical drying-wetting  
 540 cycles, occurring at relatively low stresses in earth structures after compaction, on the hydraulic behaviour of a low  
 541 activity compacted clayey silt used for the construction of water defenses, and to explain the observed behaviour with  
 542 the aid of microstructural evidences.

543 While the overall volume strains were negligible and became reversible after a limited number of drying-wetting cycles,  
 544 the hydraulic behaviour was dramatically affected by the hydraulic history in which water retention capacity reduced  
 545 and hydraulic conductivity increased. The fabric of the tested soil consists of peds of clay particles mixed among silt  
 546 grains, with larger pores external to the peds and smaller pores within the peds. Microstructural investigation, based on  
 547 MIP analyses, indicated that the porosity and the volume of the peds decreased mainly during the first cycles.

548 Meanwhile, the fraction of porosity external to the peds increased since the overall volume remained almost constant.  
 549 Thus, the repeated hydraulic loads induced a sort of hydraulic fabric degradation associated to the development of  
 550 larger pores.

551 A double porosity model, calibrated on the microstructural observations and accounting for coupling between the  
 552 hydraulic and mechanical responses, was developed. An important feature of the model was introducing an elasto-  
 553 plastic behaviour for the clay aggregates, which is usually neglected in similar formulations. Good reproduction of the  
 554 experimental results was obtained by imposing the dependency of the water retention on the intra-peds and  
 555 macrostructural void ratios, whose evolution is governed by suction and degree of saturation. Besides, the substantial  
 556 change in hydraulic conductivity observed at the sample level was explained by means of the fabric changes predicted  
 557 by the proposed modelling framework. As the soil tested is a low plasticity clayey silt, its behaviour is hardly affected  
 558 by the sensitivity to water of the constituent minerals, contrarily to active clays. Nonetheless, this investigation shows  
 559 that the irreversible hydromechanical behaviour of the peds causes substantial changes in the water retention capacity as  
 560 well as in the hydraulic conductivity of this material. These changes should be considered when the assessment of the  
 561 hydromechanical behaviour of soils used in earth constructions is required for the design lifetime, since the response of  
 562 the construction will not be governed only by the soil fabric at the time of compaction.

563

## 564 REFERENCES

- 565 Airò Farulla, C., Ferrari, A. and Romero, E. 2010. Volume change behaviour of a compacted silty clay during cyclic  
 566 suction changes. *Canadian Geotechnical Journal*, 47(6): 688-703.
- 567 Albrecht, B. and Benson, C. 2001. Effect of desiccation on compacted natural clays. *Journal of Geotechnical and*  
 568 *Geoenvironmental Engineering*, 127(1): 67–76.
- 569 Albright, W. H., Benson, C. H., Gee, G. W., Roesier, A. C., Abichou, T., Apiwantragoon, P., Lyles, B. F. and Rock, S.  
 570 A. 2004. Field water balance of landfill final covers. *Journal of Environmental Quality*, 33(6): 1–17.
- 571 Alonso, E. E., Romero, E., Hoffmann, C. and García-Escudero, E. 2005. Expansive bentonite–sand mixtures in cyclic  
 572 controlled-suction drying and wetting. *Engineering Geology*, 81: 213–226.
- 573 Alonso, E. E., Vaunat, J. and Gens, A. 1999. Modelling the mechanical behaviour of expansive clay. *Engineering*  
 574 *Geology*, 54: 173–183.
- 575 Alshihabi, O., Shahrour, I. and Mieussens, C. 2002. Experimental study of the influence of suction and drying/wetting  
 576 cycles on the compressibility of a compacted soil. *Proceedings of 1st International Conference on Unsaturated Soils*,  
 577 Balkema, Rotterdam, The Netherlands, pp. 541–545.
- 578 Aubertin, M., Mbonimpa, M., Bussière, B. and Chapuis, R. 2003. A model to predict the water retention curve from  
 579 basic geotechnical properties. *Canadian Geotechnical Journal*, 40: 1104–1122.
- 580 Azizi, A. 2016. Effects of hydraulic repeated loads on the hydromechanical response of an unsaturated silty soil. PhD  
 581 Thesis, Politecnico di Milano.
- 582 Azizi, A., Jommi, C. and Musso, G. 2017. A water retention model accounting for the hysteresis induced by hydraulic  
 583 and mechanical wetting-drying cycles. *Computers and Geotechnics*, 87: 86-98.

- 584 Azizi, A., Musso, G., Jommi, C. and Cosentini, R. M. 2018. Evolving fabric and its impact on the shearing behaviour of  
585 a compacted clayey silt exposed to drying-wetting cycles. *Proceedings of 7th international conference on unsaturated*  
586 *soils (UNSAT2018)*, Hong Kong, pp. 641-646.
- 587 Bear, J. 1972. *Dynamics of Fluids in Porous Materials*. American Elsevier.
- 588 Benson, C. and Khire, M. 1995. Earthen covers for semi-arid and arid climates. *Landfill Closures*, J. Dunn and U. Singh  
589 eds., ASCE, New York, 201–217.
- 590 Benson, C. H., Sawangsuriya, A., Trzebiatowski, B. and Albright, W. H. 2007. Postconstruction changes in the  
591 hydraulic properties of water balance cover soils. *Journal of Geotechnical and Geoenvironmental Engineering*, 133(4):  
592 349–359.
- 593 Bishop, A. 1959. The principle of effective stress. *Tecnisk Ukeblad*, 39: 859–863.
- 594 Calabresi, G., Colleselli, F., Danese, D., Giani, G. P., Mancuso, C., Montrasio, L., Nocilla, A., Pagano, L., Reali, E. and  
595 Sciotti A. 2013. A research study of the hydraulic behaviour of the Po river embankments. *Canadian Geotechnical*  
596 *Journal*, 50(9): 947-960.
- 597 Casini, F., Vaunat, J., Romero, E. and Desideri, A. 2012. Consequences on water retention properties of double-porosity  
598 features in a compacted silt. *Acta Geotechnica*, 7(2): 139–150.
- 599 Chapuis, 2002. Full-scale hydraulic performance of soil–bentonite and compacted clay liners. *Canadian Geotechnical*  
600 *Journal*, 39 (2): 417–439.
- 601 Croney, D. 1977. *The design and performance of road pavements*. London: Her Majesty's Stationery Office.
- 602 Cui, Y. J., Loiseau, C. and Delage, P. 2002. Microstructure changes of a confined swelling soil due to suction controlled  
603 hydration. *Proceeding of 3rd Int. Conf. on Unsaturated Soils (UNSAT 2002)*, Recife, Brazil (ed. Jucá, J. F. T., de  
604 Campos, T. M. P. and Marinho, F. A. M.), Lisse: Swets and Zeitlinger, Vol. 2, pp. 593-598.
- 605 Cuisinier, O., Auriol, J. C., Tangi, L. B. and Dimitri, D. 2011. Microstructure and hydraulic conductivity of a  
606 compacted lime-treated soil. *Engineering Geology*, 123 (3): 187–193
- 607 Cuisinier, O. and Masrouri, F. 2005. Hydromechanical behaviour of a compacted swelling soil over a wide suction  
608 range. *Engineering Geology*, 81: 204–212.
- 609 Daniel, D. E. 1987. Earthen liners for land disposal facilities. *Geotech. Practice for Waste Disposal*. No. 13, R. D.  
610 Woods, ed., Ann Arbor, Mich., 21–39.
- 611 Delage P. and Lefebvre G. 1984. Study of the structure of a sensitive Champlain clay and of its evolution during  
612 consolidation. *Canadian Geotechnical Journal*, 21(1): 21–35.
- 613 Delage, P. and Pellerin, F.M. 1984. Influence de la lyophilisation sur la structure d'une argile sensible du Québec. *Clay*  
614 *Minerals*, 19: 151-160.
- 615 Della Vecchia, G., Dieudonne, A. C., Jommi, C. and Charlier, R. 2015. Accounting for evolving pore size distribution  
616 in water retention models for compacted clays. *International Journal for Numerical and Analytical Methods in*  
617 *Geomechanics*, 39 (7): 702-723.
- 618 Della Vecchia, G., Jommi, C. and Romero E. 2013. A fully coupled elastic–plastic hydromechanical model for  
619 compacted soils accounting for clay activity. *International Journal for Numerical and Analytical Methods in*  
620 *Geomechanics*, 37 (5): 503–535.
- 621 Drumm, E., Boles, D. and Wilson, G. 1997. Desiccation cracks result in preferential flow. *Geotech. News*, 152: 22–25.
- 622 Durner W. 1994. Hydraulic conductivity estimation for soils with heterogeneous pore structure. *Water Resources*  
623 *Research*, 30(2): 211–223
- 624 Eching, S. O. and Hopmans, J. W. 1993. Optimization of Hydraulic Functions from Transient Outflow and Soil Water  
625 Pressure Data. *Soil Science Society of America Journal*, Vol. 57, pp. 1167–1175.
- 626 Fleureau J. M., Verbrugge J. C. , Huergo P. J. , Correia A. G. , Kheirbek-Saoud S. 2002. Aspects of the behaviour of  
627 compacted clayey soils on drying and wetting paths. *Canadian Geotechnical Journal*, 39: 1341–1357.

- 628 Fredlund, D. G. and Rahardjo, H. 1993. Soil Mechanics for Unsaturated Soils. John Wiley and Sons, Inc., Hoboken, NJ,  
629 USA. doi: 10.1002/9780470172759.ch1.
- 630 Fujimaki, H. and Inoue, M. 2003. Reevaluation of the Multistep Outflow Method for Determining Unsaturated  
631 Hydraulic Conductivity. *Vadose Zone Journal*, 2, pp. 409–415.
- 632 Gens, A. and Alonso, E. E. 1992. A framework for the behaviour of unsaturated expansive clays. *Canadian*  
633 *Geotechnical Journal*, 29: 1013–1032.
- 634 Iyer, B. 1990. Pore water extraction – comparison of saturation extract and high-pressure squeezing. *Physico-chemical*  
635 *Aspects of Soils and Related Materials – ASTM STP 1095 K.P. Hoddinot and R.O. Lamb (eds), Philadelphia*, 159-170.
- 636 Jommi, C. 2000. Remarks on the constitutive modelling of unsaturated soils. In *Experimental Evidence and Theoretical*  
637 *Approaches in Unsaturated Soils*, Tarantino A, Mancuso C (eds.). AA. Balkema, Rotterdam, 139–153.
- 638 Koliji, A., Vulliet, L. and Laloui, L. 2010. Structural characterization of unsaturated aggregated soil. *Canadian*  
639 *Geotechnical Journal*, 47(3): 297-297.
- 640 Leong, E., He, L. and Rahardjo, H. 2002. Factors Affecting the Filter Paper Method for Total and Matric Suction  
641 Measurements. *Geotechnical Testing Journal* 25(3): 322-333.
- 642 Lloret, A., Villar, M. V., Sanchez, M., Gens, A., Pintado, X. and Alonso, E. E. 2003. Mechanical behaviour of heavily  
643 compacted bentonite under high suction changes. *Géotechnique*, 53 (1): 27–40.
- 644 Mašin, D. 2013. Double structure hydromechanical coupling formalism and a model for unsaturated expansive clays.  
645 *Engineering Geology*, 165: 73–88.
- 646 Mualem, Y. 1976. A new model for predicting the hydraulic conductivity of unsaturated porous media. *Water*  
647 *Resources Research*, 12(3): 513–522.
- 648 Musso, G., Romero, E. and Della Vecchia, G. 2013. Double-structure effects on the chemo-hydromechanical behaviour  
649 of a compacted active clay, *Géotechnique*, 15: 206-220.
- 650 Nocilla, A., Coop, M. R. and Colleselli, F. 2006. The mechanics of an Italian silt and example of “transitional”  
651 behaviour. *Géotechnique*, 56(4): 261-271.
- 652 Nowamooz, H. and Masrouri, F. 2009. Density-dependent hydromechanical behaviour of a compacted expansive soil.  
653 *Engineering Geology*, 106: 105–115.
- 654 Rojas J.C, Mancuso C. and Danese D. 2010. Pre and post-construction characterization of an embankment fill material.  
655 *Proceedings of the 4th Asia Pacific conference on unsaturated soils*, Newcastle, Australia, 23-25 November 2009,  
656 Buzzi O. Fytus S. and Sheng D. editors, CRC press.
- 657 Romero, E., Gens, A. and Lloret, A. 1999. Water permeability, water retention and microstructure of unsaturated  
658 compacted Boom clay. *Engineering Geology*, 54: 117-127.
- 659 Romero, E. 2013. A microstructural insight into compacted clayey soils and their hydraulic properties. *Engineering*  
660 *Geology*, 165: 3–19.
- 661 Romero, E., Della Vecchia, G. and Jommi, C. 2011. An insight into the water retention properties of compacted clayey  
662 soils. *Géotechnique*, 61(4): 313–328.
- 663 Romero, E. and Jommi, C. 2008. An insight into the role of hydraulic history on the volume changes of anisotropic  
664 clayey soils. *Water Resources Research*, 44, W12412:1–W12412:16.
- 665 Romero, E. and Vaunat, J. 2000. Retention curves of deformable clays. proc. int. workshop on unsaturated soils. In  
666 Tarantino, A. and Mancuso, C., editors, *Experimental Evidence and Theoretical Approaches in Unsaturated Soils*, 91–  
667 106, Trento, Italy. AA. Balkema, Rotterdam.
- 668 Romero, E., Vaunat, J. and Merchan V. 2014. Suction effects on the residual shear strength of clays. *Journal of Geo-*  
669 *Engineering Sciences* 2 (2014) 17–37. doi:10.3233/JGS-141320.
- 670 Rouainia, M., Davies, O., O’Brien, T. and Glendinning, S. 2009. Numerical modelling of climate effects on slope  
671 stability. *Proceedings of the Institution of Civil Engineers – Engineering Sustainability*, 162(2): 81–89.

- 672 Sharma, R. S. (1998). Mechanical behaviour of unsaturated highly expansive clays. PhD Thesis, Oxford University.
- 673 Smethurst, J. A., Clark, D. and Powrie, W. 2006. Seasonal changes in pore water pressure in a grass-covered cut slope  
674 in London Clay. *Géotechnique*, 56 (8): 523-537.
- 675 Tarantino A., De Col S. 2008. Compaction behaviour of clay. *Géotechnique*, 58 (3): 199–213.
- 676 U.S. Department of Agriculture (USDA) 1950. Diagnosis and improvement of saline and alkali soils, Agricultural  
677 Handbook No. 60, USDA, Washington, DC.
- 678 van Dam, J. C., Stricker, J. N. M. and Droogers, P. 1994. Inverse Method to Determine Soil Hydraulic Functions from  
679 Multistep Outflow Experiments. *Soil Science Society of America Journal*, Vol. 58, pp. 647– 652.
- 680 Van Genuchten, M. T. 1980. A closed-form equation for predicting the hydraulic conductivity of unsaturated soils. *Soil*  
681 *Science Society of America Journal*, 44: 892–898.
- 682 Vassallo, R., Mancuso, C. and Vinale, F. 2007. Effects of net stress and suction history on the small strain stiffness of a  
683 compacted clayey silt. *Canadian Geotechnical Journal*, 44(4): 447-462
- 684 Vaughan, P. R., Kovacevic, N. and Potts, D. M. 2004. Then and now: some comments on the design and analysis of  
685 slopes and embankments. *Advances in Geotechnical Engineering: Proceedings of the Skempton Conference, Imperial*  
686 *College*, London, Vol. 1, pp. 241–290.
- 687 Wang G., Wei X. 2015. Modeling swelling–shrinkage behavior of compacted expansive soils during wetting–drying  
688 cycles. *Canadian Geotechnical Journal*, 52 (6): 783 – 79.
- 689  
690 Wheeler, S. J., Sharma, R. S. and Buisson, M. S. R. 2003. Coupling of hydraulic hysteresis and stress-strain behaviour  
691 in unsaturated soils. *Géotechnique* 53(1): 41-54.
- 692  
693  
694  
695  
696  
697

#### 698 **List of Tables**

- 699 Table 1. Properties of the tested soil
- 700 Table 2. Properties of the as-compacted specimens
- 701 Table 3. The description of the tests carried out
- 702 Table 4. Threshold pore radii and micro-structural, meso-structural and macro-structural void ratios
- 703 Table 5. Parameters of the water retention model
- 704 Table 6. Parameters of the mechanical model
- 705
- 706 **List of Figures**
- 707 Figure 1. Grain size distribution of the tested material
- 708 Figure 2. Water content changes during drying and wetting paths
- 709 Figure 3. Mechanical response to repeated hydraulic loads: Volumetric strain with number of cycles

- 710 Figure 4. Effect of repeated hydraulic loads on the water retention behaviour: (a)  $S_r$ -log( $s$ ) (b)  $e$ -log( $s$ ) (c)  $e_w$ -log( $s$ )
- 711 Figure 5. (a) Changes in volumetric water content: experimental data and inverse modeling (b) Unsaturated hydraulic  
712 conductivity of the as-compacted and 6D/W specimens
- 713 Figure 6. ESEM photomicrographs: (a) Particles, peds and macropores (b) Macropores and ped (c) Mesopores (d) Ped  
714 breakage after drying-wetting cycles
- 715 Figure 7. Effect of repeated hydraulic loads on MIP results: (a) Evolution of pore size density function (b) Evolution of  
716 intruded void ratio
- 717 Figure 8. Comparison between the experimental and MIP derived WRCs
- 718 Figure 9. Hydromechanical model proposed to reproduce the behaviour of the peds: (a) Yield surfaces in  $\sigma'_{m-s}$  plane (b)  
719 Influence of plastic strains on the water retention curve
- 720 Figure 10. Comparing model predictions and experimental data in terms void ratio and suction: (a) Total void ratio  
721 suction (b) Evolution of  $e_{Ma}$  and  $e_m$  with suction
- 722 Figure 11. Comparing model predictions and experimental data in terms of  $S_r$ -log( $s$ ): (a) for the as-compacted specimen  
723 (b) evolution of  $S_{rMa}$  and  $S_{rm}$  during repeated hydraulic loads (c) for the 6D/W specimen
- 724 Figure 12. Comparing model predictions and experimental data in terms of  $e_w$ -log( $s$ ) for: (a) as-compacted specimen  
725 (b) 6D/W specimen
- 726 Figure 13. Hydraulic conductivity predicted by the proposed model: (a)  $k_r$ - $S_e$  (b)  $K_w$ - $S_e$
- 727
- 728
- 729
- 730
- 731
- 732
- 733
- 734
- 735
- 736
- 737
- 738

**NOTATION**

$A$ , Activity

$B$ , parameter of Kozeny-Carman equation

$C(s)$ , moisture capacity

$e$ , void ratio

$e_{int}$ , intruded void ratio

$e_{Ma}$ , macrostructural void ratio

$e_{Ma0}$ , initial macrostructural void ratio

$e_{Me}$ , mesostructural void ratio

$e_{Mi}$ , microstructural void ratio

$e_m$ , intra-peds void ratio

$e_{m0}$ , initial intra-peds void ratio

$e_w$ , water ratio

$e_w^{sc}$ , water ratio in scanning domain

$e_{wMa}$ , macrostructural water ratio

$e_{wMa}^{sat}$ , saturated water ratio of macropores

$e_{wm}$ , intra-peds water ratio

$e_{wm}^{sat}$ , saturated water ratio of peds

$G_s$ , Specific Density

$h_{LC}$ , model parameter controls the coupled movement of LC due to SI or SD yielding

$h_s$ , model parameter controls the coupled movement of SI and SD due to LC yielding

$K_s$ , saturated hydraulic conductivity

$K_w$ , hydraulic conductivity

$k_r$ , relative permeability

$k_{sc}$ , model parameter controlling the slope of the scanning curves

$LC$ , loading collapse yield curve

$LL$ , Liquid limit

$n_{Ma}$ ,  $m_{Ma}$ ,  $\alpha_{Ma}$ , parameters of van Genuchten model for macropores

$n_m, m_m, \alpha_m$ , parameters of van Genuchten model for intra-peds pores

$p(S_{r-int})$ , intruded pressure

$PI$ , plastic index

$r$ , apparent pore radius

$R_{Me}$ , threshold pore radius separating macropores from mesopores

$R_{Mi}$ , threshold pore radius separating micropores from mesopores

$RH$ , Relative Humidity

$s$ , suction

$s_I$ , suction increase yield suction

$s_D$ , suction decrease yield suction

$S_e$ , effective degree of saturation

$S_r$ , degree of saturation

$S_{res}$ , residual degree of saturation

$S_{rMa}$ , macrostructural degree of saturation

$S_{rm}$ , intra-peds degree of saturation

$S_{r-int}$ , normalized intruded volume

$T$ , temperature

$t$ , time

$V_s$ , volume of the solid phase

$V_{vMa}$ , volume of macropores

$V_{vMe}$ , volume of mesopores

$V_{vMi}$ , volume of micropores

$V_{vm}$ , intra-peds voids

$V_{wMa}$ , volume of water within macropores

$V_{wm}$ , volume of water within peds

$w$ , water content

$\varepsilon_v$ , volumetric strain

$\varepsilon_m^e$ , elastic volumetric strain of peds

$\varepsilon_m^p$ , plastic volumetric strains of peds

$\gamma_w$ , specific weight of water

$\kappa$ , model parameter controlling the slope of unloading-reloading curve for soil

$\kappa_m$ , model parameter controlling the slope of unloading-reloading curve for peds

$\lambda_m$ , model parameter controlling the slope of normal compression line for peds

$\theta$ , volumetric water content

$\rho_d$ , dry density

$\sigma_{net}$ , net stress

$\sigma_v^{net}$ , axial net stress

$\sigma'$ , effective stress

$\sigma'_{Ma}$ , macrostructural effective stress

$\sigma'_m$ , peds effective stress

$\sigma'^*_m$ , peds preconsolidation stress

$1/\alpha_m$ , air-entry value of peds

$1/\alpha_{Ma}$ , air-entry value of macropores

$1/\alpha_{m0}$ , initial air-entry value of peds

$1/\alpha_{Ma0}$ , initial air-entry value of macropores

Table 1. Properties of the tested soil

Variables	Value
Liquid limit $LL$ (%)	32.6
Plastic limit $PL$ (%)	24.3
Plasticity Index $PI$ (%)	8.3
Activity $A$ (-)	0.4
Specific Density $G_s$	2.735
Clay fraction ( $d < 2\mu\text{m}$ , %)	20.4
$\text{CaCO}_3$ content (%)	17.3

Table 2. Properties of the as-compacted specimens

Condition	$\rho_d$ (kg/m <sup>3</sup> )	$e$ (-)	$w$ (%)	$S_r$ (-)	$s$ (kPa)
As-compacted	$1650 \pm 10$	$0.66 \pm 0.01$	$20 \pm 0.2$	$0.83 \pm 0.02$	33

Table 3. List of hydraulic and microstructural tests carried out with reference to figures

Type of test and figure	Method	Sample type
Water retention (Fig. 5)	Axis Translation, Vapour Equilibrium	As-compacted, 3D/W, 6D/W
Saturated hydraulic conductivity (Fig. 6, Fig. 14)	Constant head	As-compacted, 1D/W, 3D/W, 6D/W
Unsaturated hydraulic conductivity (Fig. 6, Fig. 14)	Back analysis of Richard's equation	As-compacted, 6D/W
Micro-photograph (Fig. 7)	Environmental Scanning Electron Microscopy	As-compacted, 6D/W
Pore Size Distribution and Pore Size Density (Fig. 8)	Mercury Intrusion Porosimetry	As-compacted, as compacted dry, 6D/W dry, 6D/W

Table 4. Threshold pore radii and micro-structural, meso-structural and macro-structural void ratios

void ratio	Lower threshold pore radius (nm)				Void ratio			
	As-compacted	First drying	6D/W dry	6D/W wet	As-compacted	First drying	6D/W dry	6D/W wet
$e_{Mi}$	-	-	-	-	0.06	0.06	0.06	0.06
$e_{Me}$	11	11	11	11	0.36	0.35	0.32	0.32
$e_{Ma}$	609	609	917	917	0.24	0.23	0.25	0.28
$e = e_{Ma} + e_{Me} + e_{Mi}$	-	-	-	-	0.66	0.64	0.63	0.66

Table 5. Parameters of the water retention model

Parameters	$1/\alpha_{Ma0}$ (kPa)	$n_{Ma}$	$m_{Ma}$	$1/\alpha_{m0}$ (kPa)	$n_m$	$m_m$
Drying	64	1.75	0.83	236	2.86	0.14
Wetting	8	2.37	0.97	34	2.61	0.12

Table 6. Parameters of the mechanical model

Parameters	$\kappa$	$\lambda_m$	$h_{lc}$	$h_s$	$\sigma'_m$ kPa	$S_I$ kPa	$S_D$ kPa
Values	0.003	0.032	4.3	0.25	657	236	10



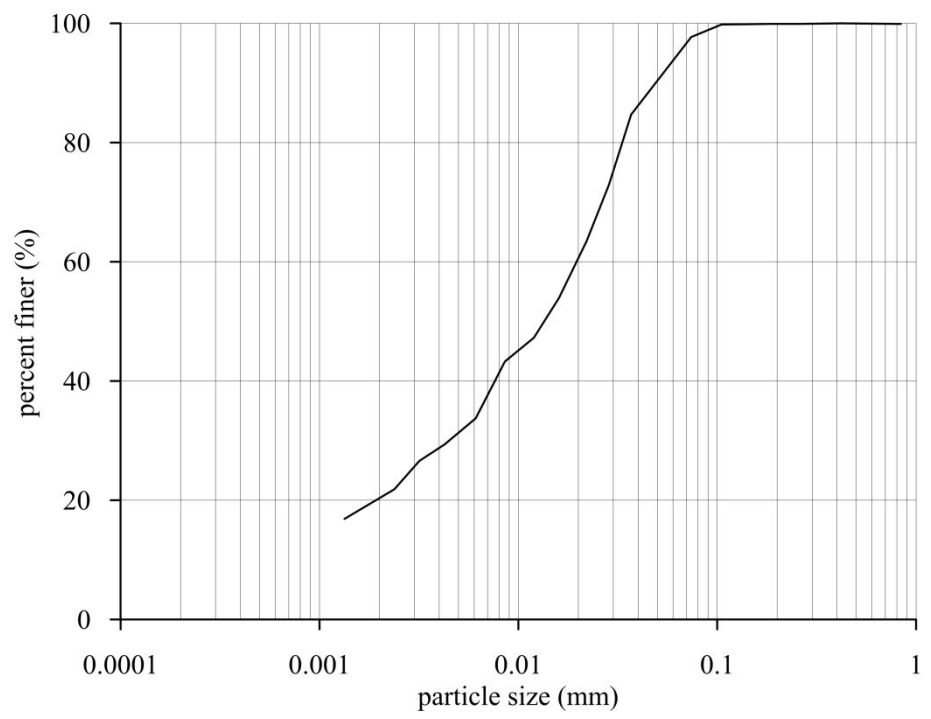


Figure 1. Grain size distribution of the tested material

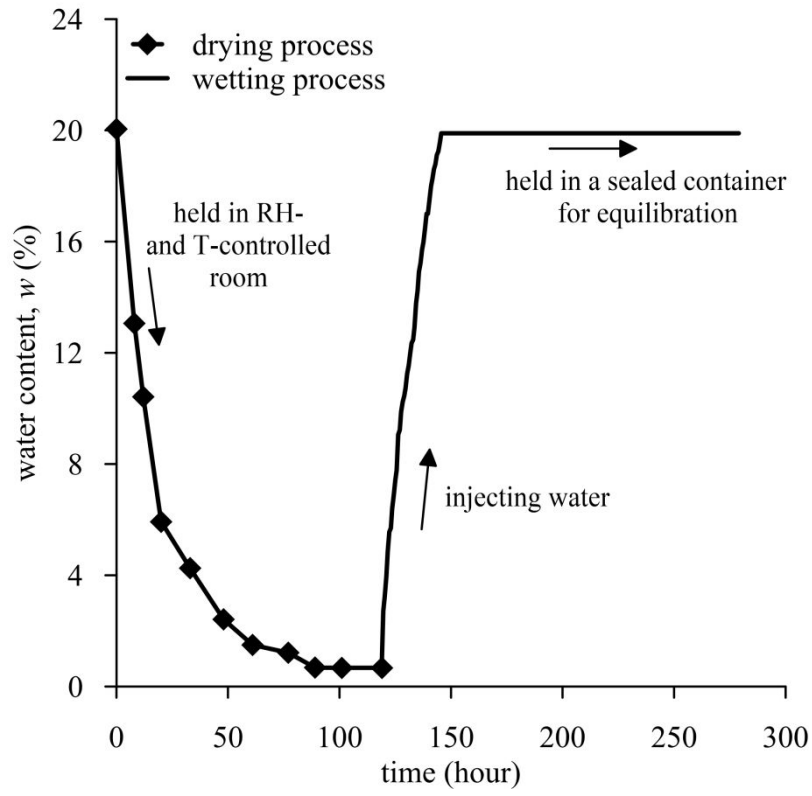


Figure 2. Water content changes during drying and wetting paths

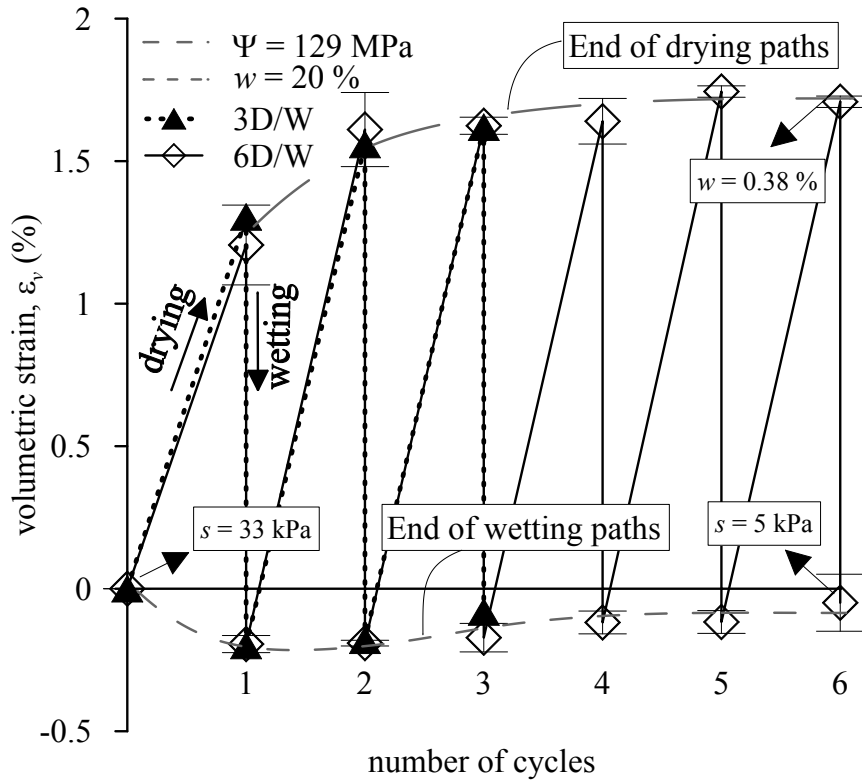


Figure 3. Mechanical response to repeated hydraulic loads: Volumetric strain with number of cycles

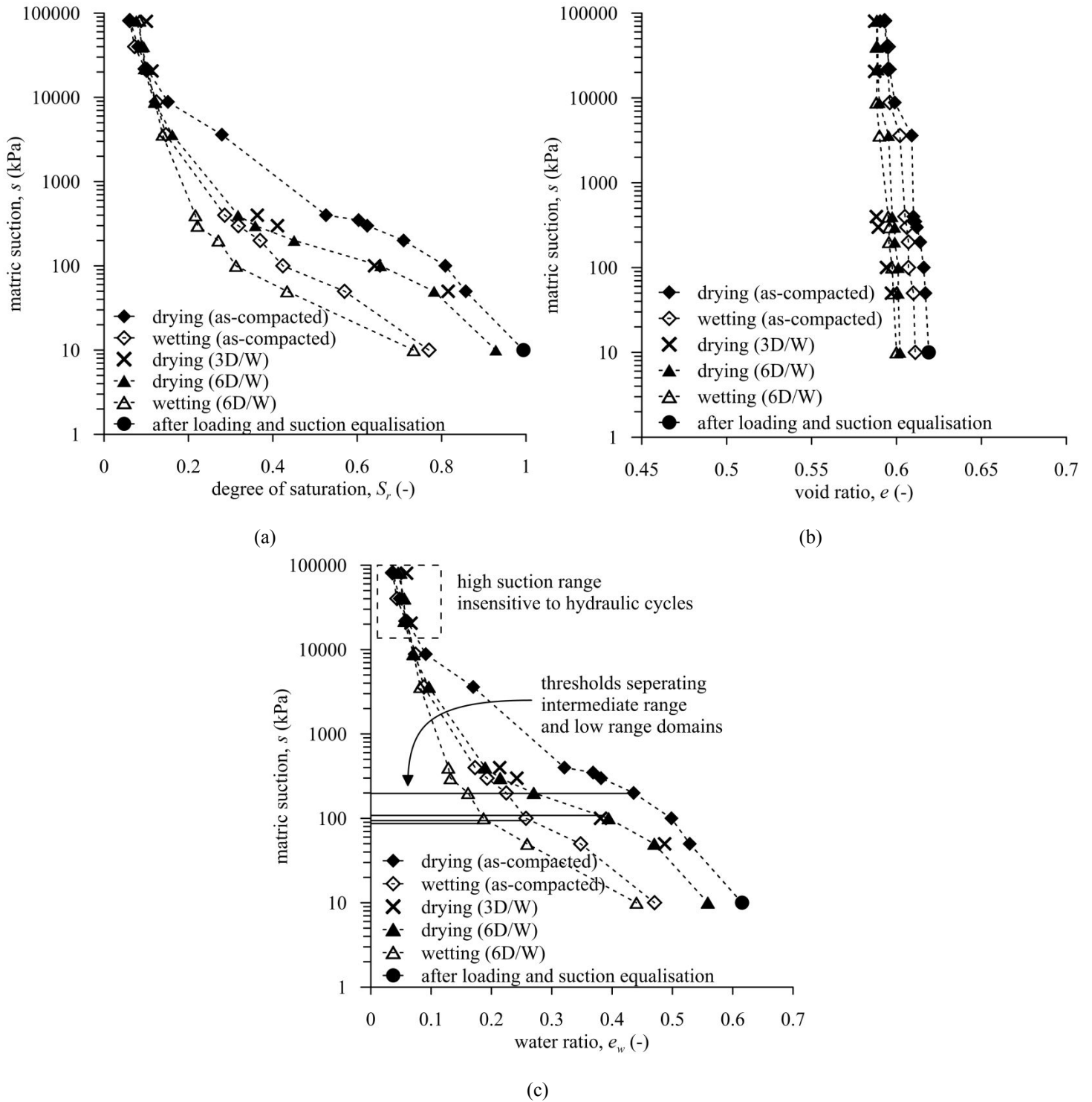


Figure 4. Effect of repeated hydraulic loads on the water retention behaviour: (a)  $S_r$ - $\log(s)$  (b)  $e$ - $\log(s)$  (c)  $e_w$ - $\log(s)$

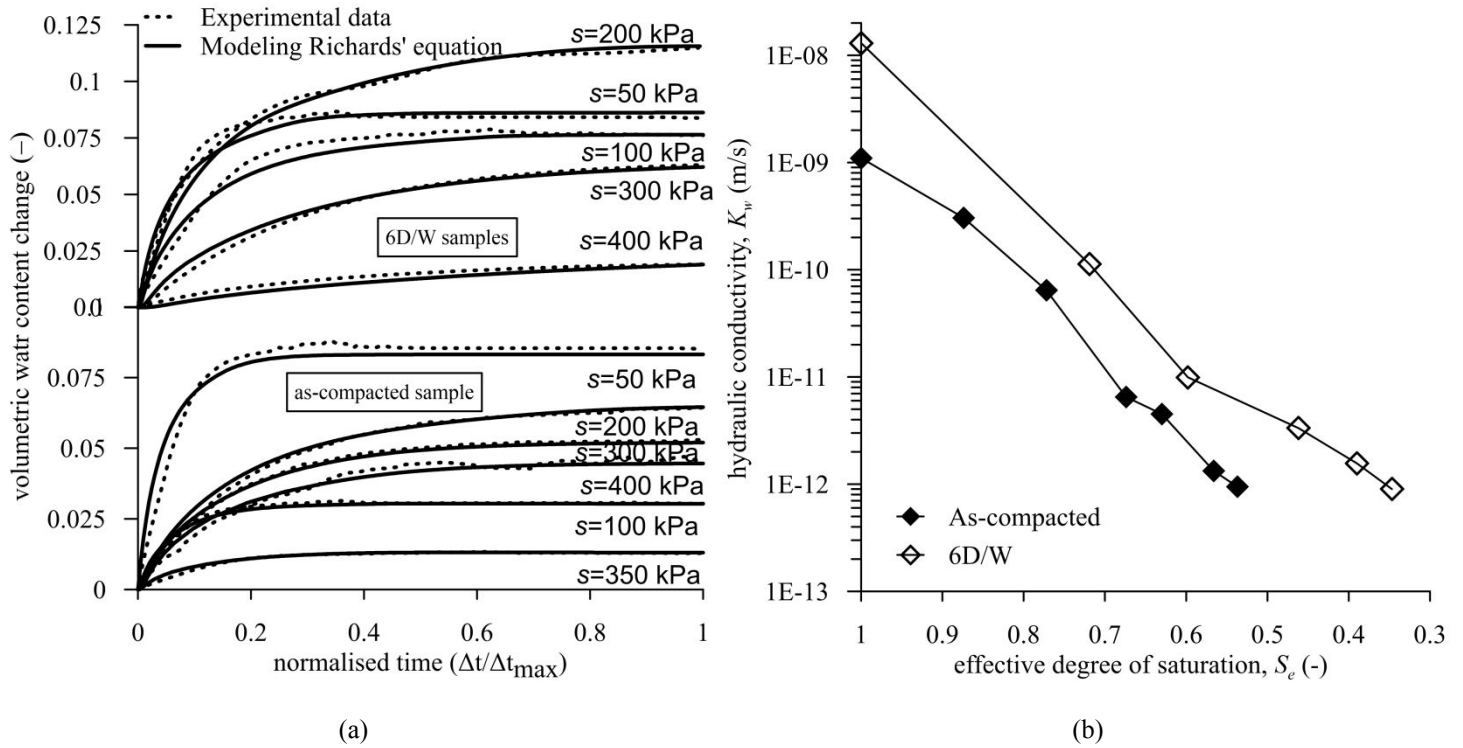


Figure 5. (a) Changes in volumetric water content: experimental data and inverse modeling (b) Unsaturated hydraulic conductivity of the as-compacted and 6D/W specimens

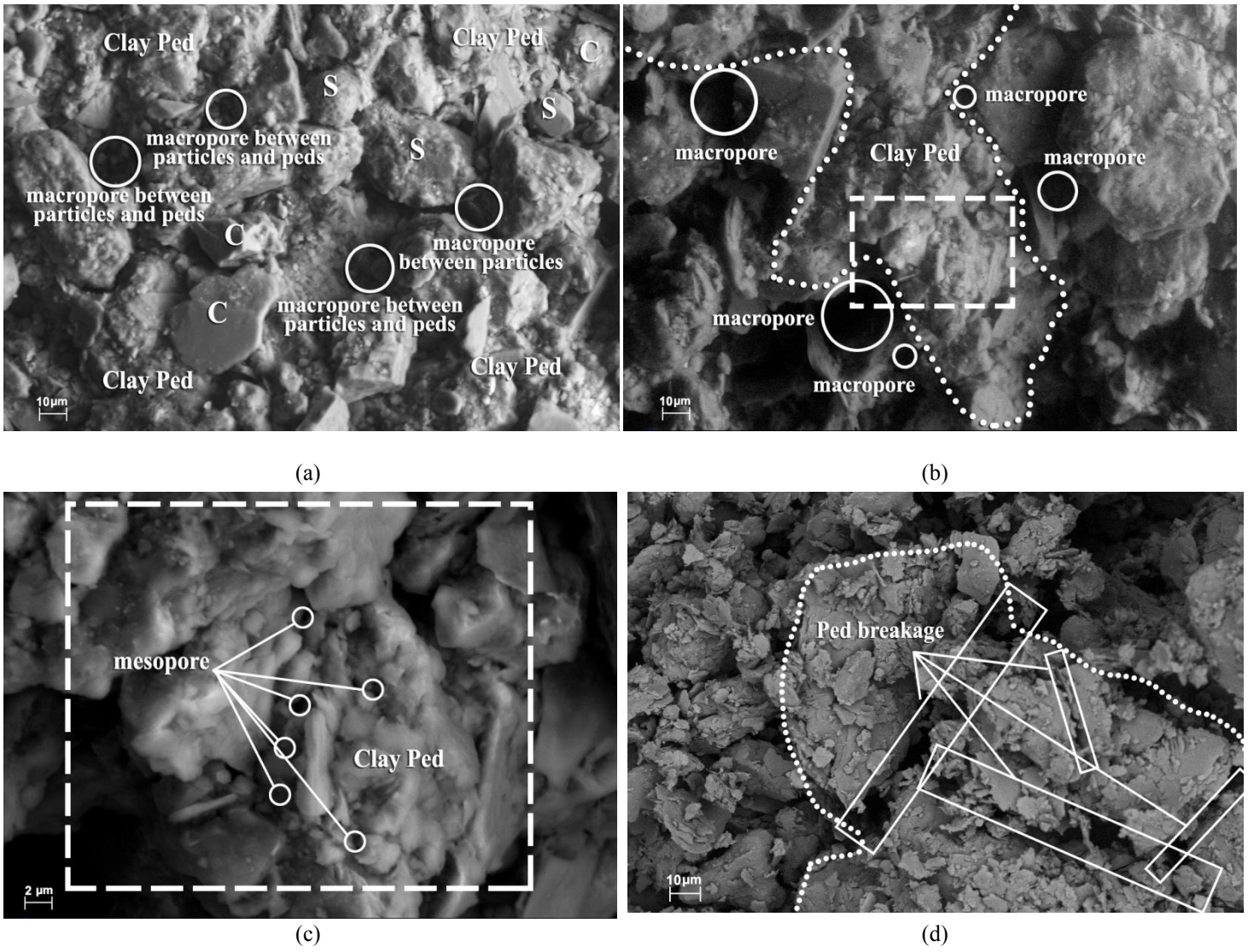


Figure 6. ESEM photomicrographs: (a) Particles, peds and macropores (b) Macropores and ped (c) Mesopores

(d) Ped breakage after drying-wetting cycles

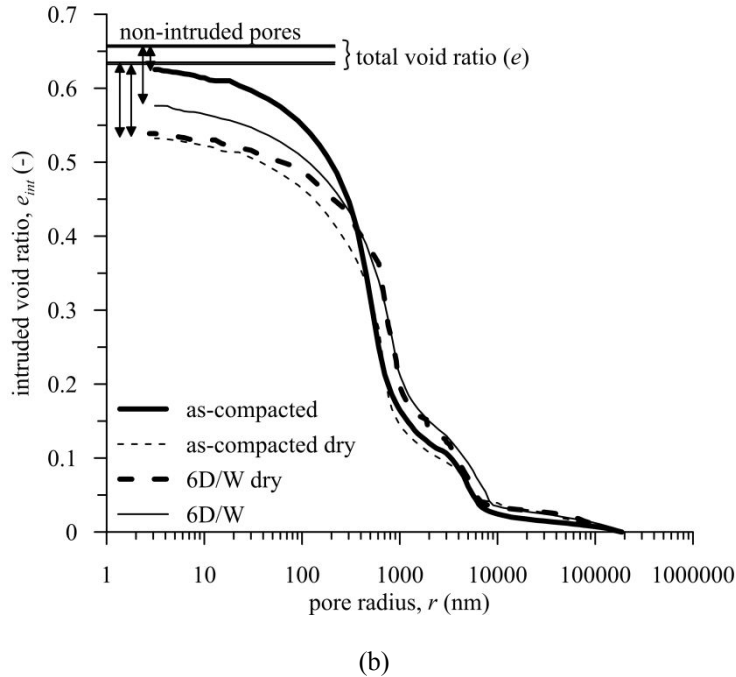
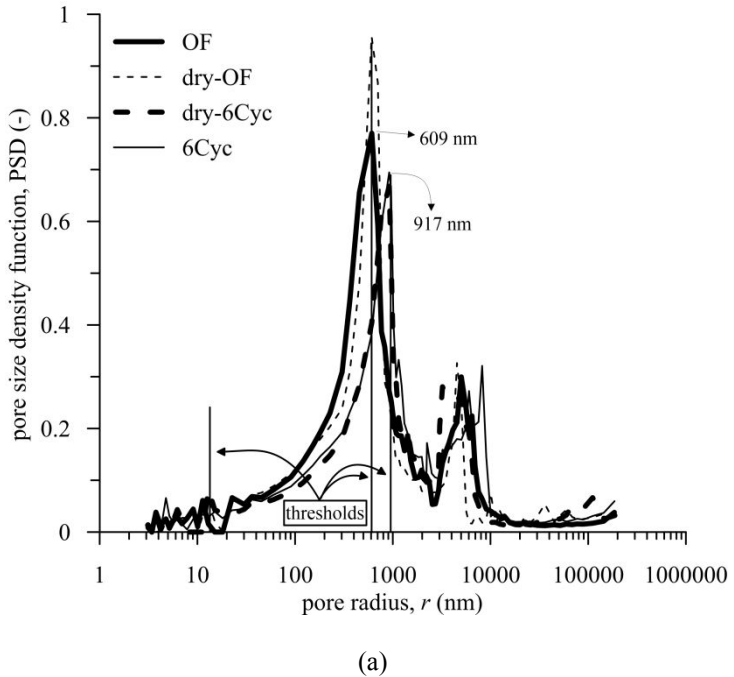


Figure 7. Effect of repeated hydraulic loads on MIP results: (a) Evolution of pore size density function (b) Evolution of intruded void ratio

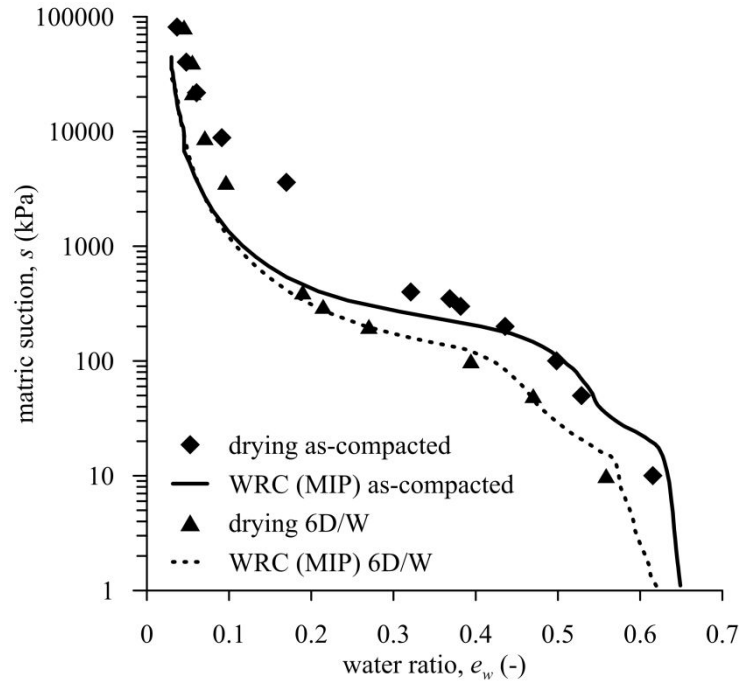


Figure 8. Comparison between the experimental and MIP derived WRCs

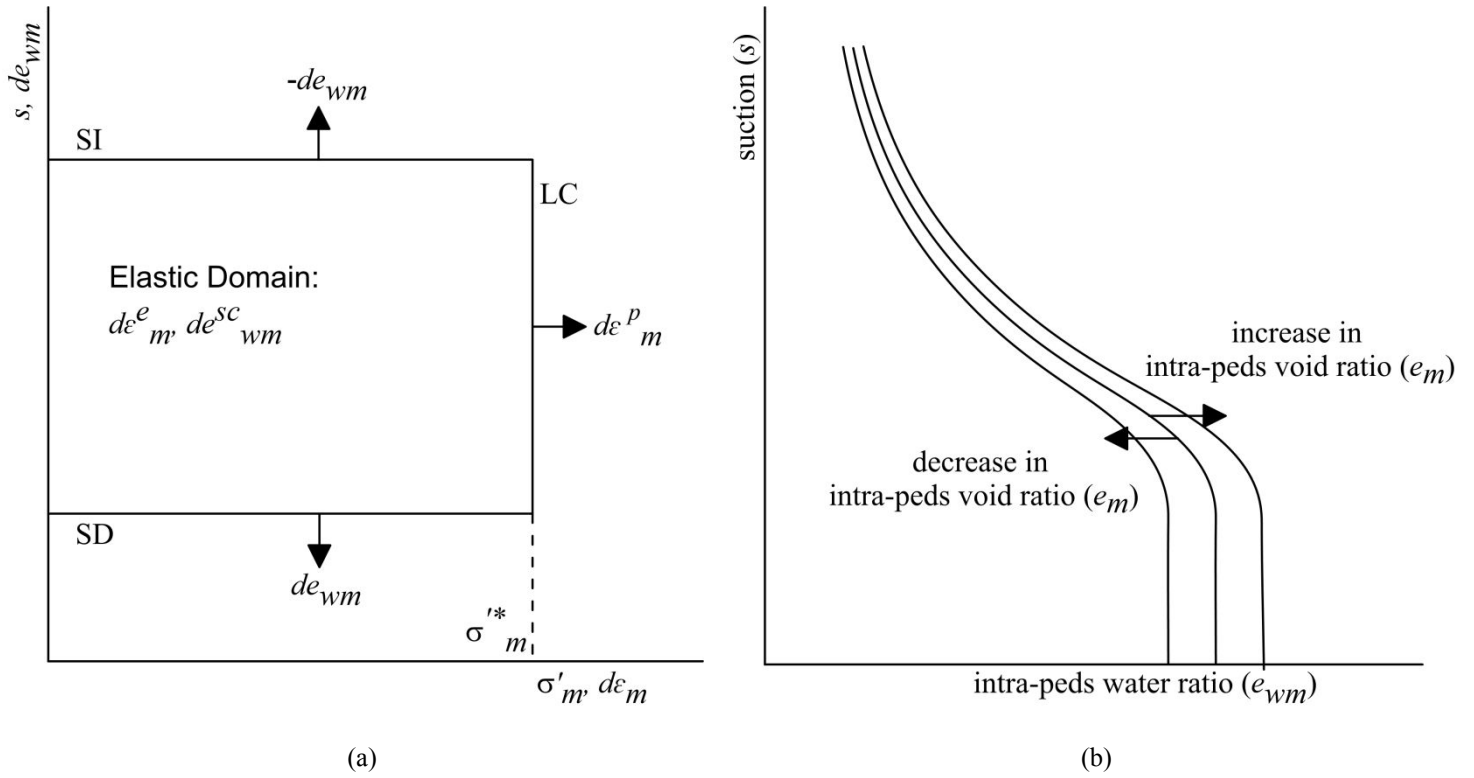


Figure 9. Hydromechanical model proposed to reproduce the behaviour of the peds: (a) Yield surfaces in  $\sigma'_m - s$  plane (b) Influence of plastic strains on the water retention curve

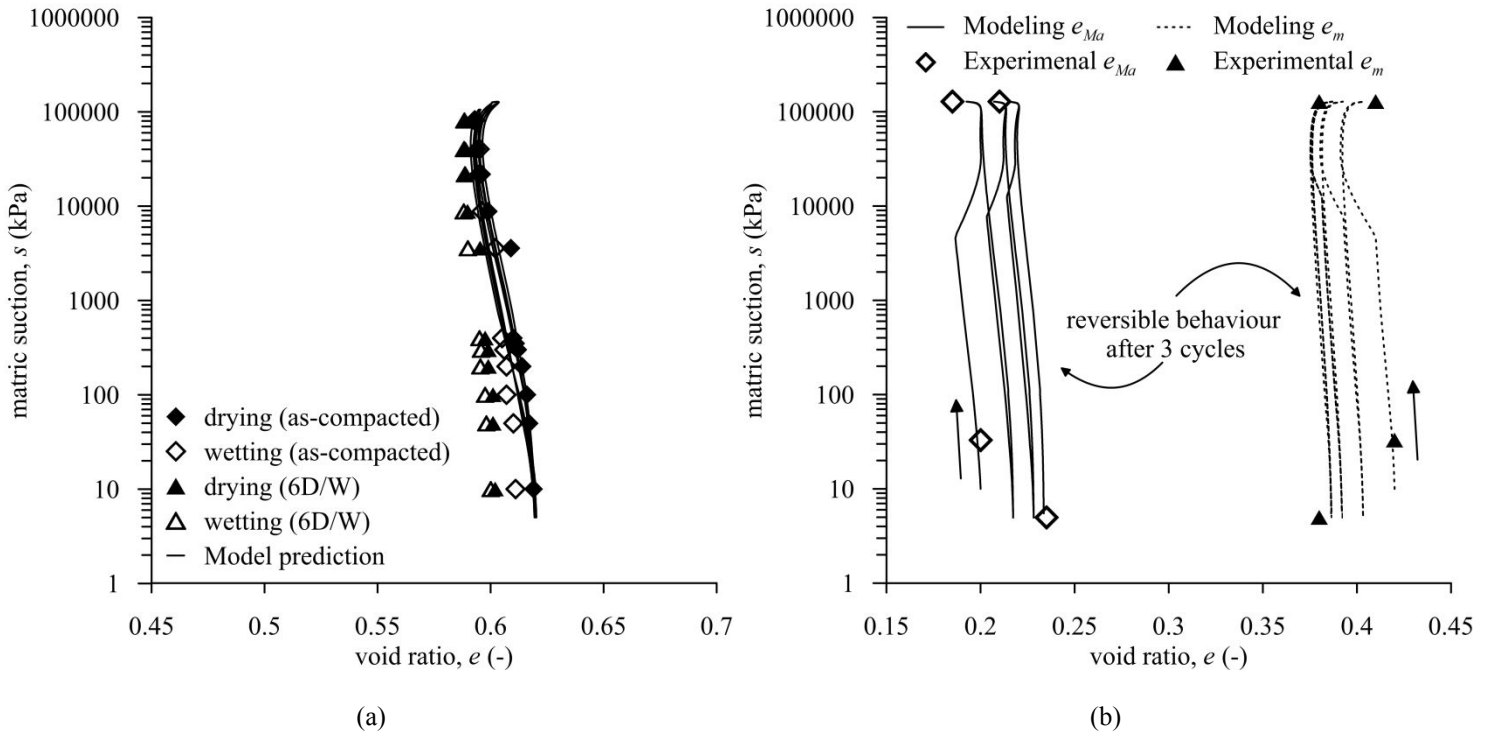


Figure 10. Comparing model predictions and experimental data in terms void ratio and suction: (a) Total void ratio suction (b)

Evolution of  $e_{Ma}$  and  $e_m$  with suction

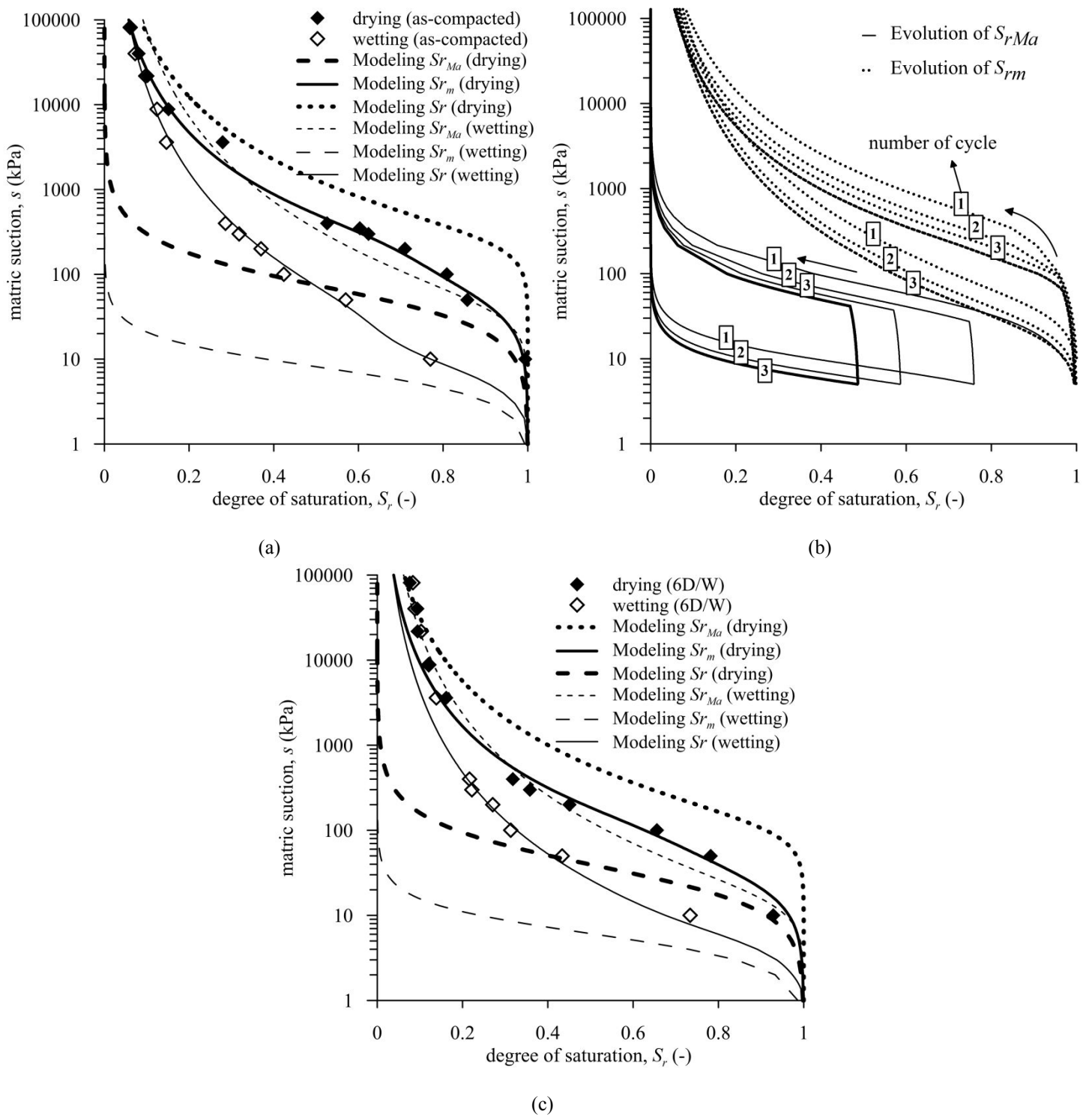


Figure 11. Comparing model predictions and experimental data in terms of  $S_r$ - $\log(S)$ : (a) for the as-compacted specimen (b) evolution of  $S_{rMa}$  and  $S_{rM}$  during repeated hydraulic loads (c) for the 6D/W specimen

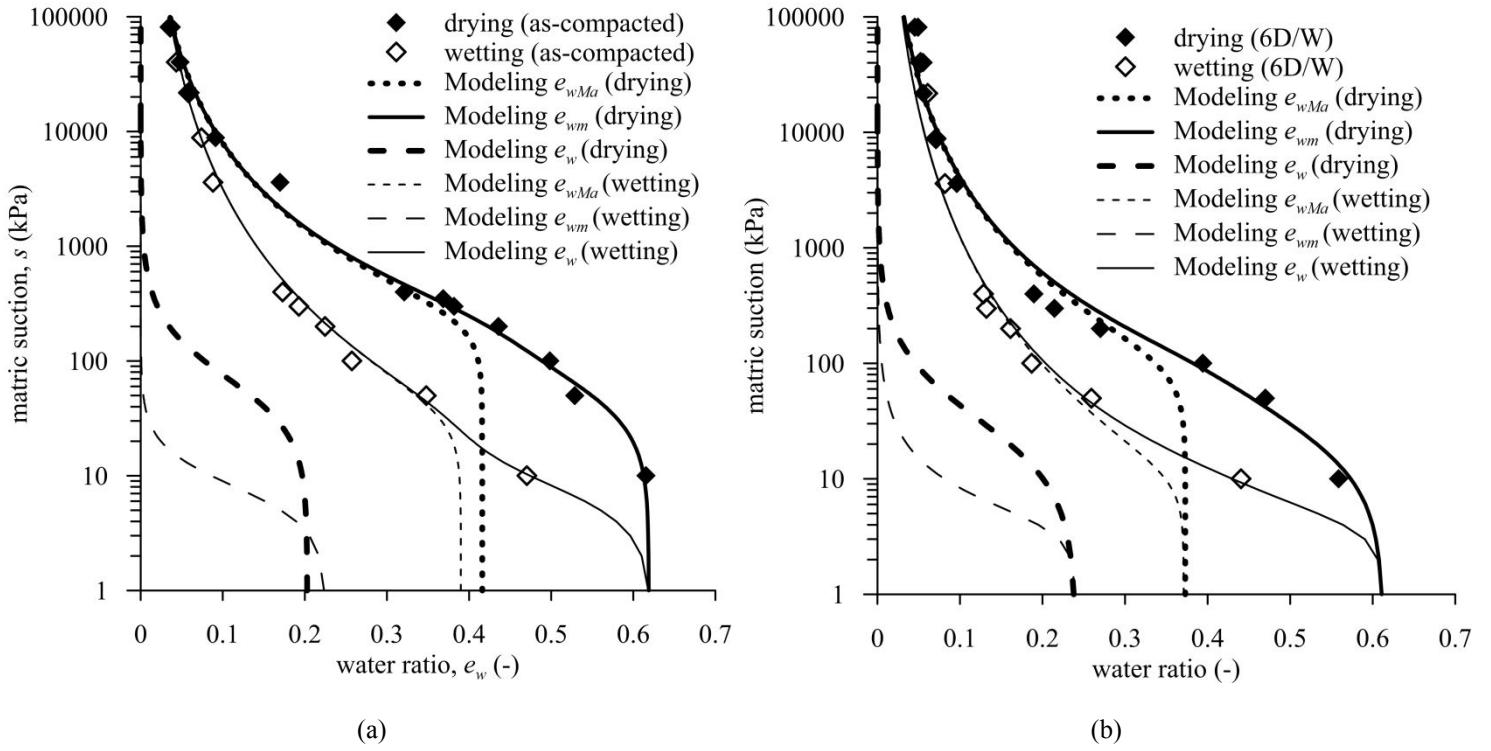


Figure 12. Comparing model predictions and experimental data in terms of  $e_w$ - $\log(s)$  for: (a) as-compacted specimen (b) 6D/W specimen

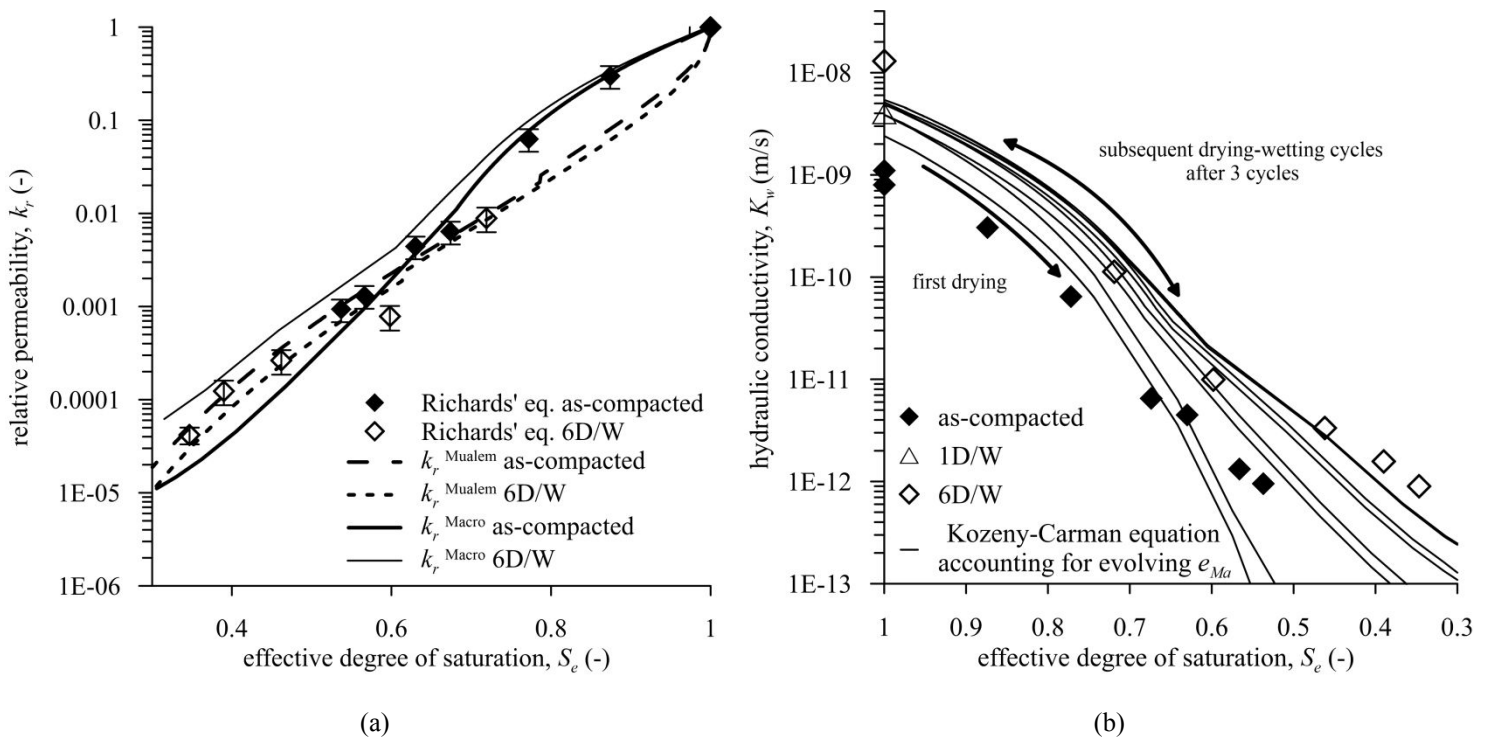


Figure 13. Permeability predicted by the proposed model: (a)  $k_r$ - $S_e$  (b)  $K_w$ - $S_e$